SCALABLE DEPOSITION METHODS FOR CARBON NANOTUBE ELECTRONICS

by

Brett A. Prussack

A thesis submitted in partial fulfillment of
the requirements for the degree of

Master of Science

(Mechanical Engineering – Research)

at the

UNIVERSITY OF WISCONSIN-MADISON

2023

Advisor Approval Page

APPROVED:

Advisor Signature	Advisor Title	Date

APPROVED:

Advisor Signature	Advisor Title	Date

APPROVED:

Advisor Signature	Advisor Title	Date

APPROVED:

Advisor Signature	Advisor Title	Date

Abstract

Carbon nanotubes (CNTs) are an advanced material with properties that show promise to advance technologies in various fields due to their unique mechanical, thermal, and electrical properties. In the field of electronics, CNTs provide a new route to manufacturing high performance transistors with exceptionally small channel lengths due to their incredible charge transport characteristics. To realize these next generation transistors, advances in manufacturing highly aligned, densely packed arrays of CNT films at scale is a necessity. Here, two solution-based deposition methods are explored and evaluated in terms of their film quality and scalability.

First, several imaging techniques used to quantify film quality are explained. Two novel methods for quantifying alignment from polarized optical microscopy (POM) images are explored. Extracting information from POM images is desirable because large areas of films can be evaluated for uniformity without the need for extensive imaging. The first technique involves rotating a sample and taking images at several rotation degrees. By dividing each image into sub-regions and evaluating the intensity as a function of rotation angle, alignment maps can be generated, and film quality assessed quickly. The second method involves taking a single POM image and evaluating intensity as a function of position. Information about alignment can be extracted from the frequency and amplitude of the resulting intensity plot.

Next, the method Tangential Flow Interfacial Self Assembly (TaFISA) is explained, and several changes to the apparatus are described. The effects of changing flow rate and lift rate are explored, and it is found that flow rate has a more significant effect on film quality than lift rate. According to this analysis, lower flow rates result in a higher number of smaller directional changes, while a larger flow rate produces films with fewer, but more drastic directional changes. Finally, demonstration of near full wafer coverage (~90%) is demonstrated on a 1x2 cm substrate.

Chapter 4 introduces a novel method for solution-based, shear-induced alignment, called oscillating shear alignment (OSA). By oscillating a substrate with a sinusoidal velocity while submerged in CNT solution, high shear rates act to align CNTs with the oscillation direction. Effects of varying the frequency and amplitude on alignment are explored, and it is found that both higher amplitudes and frequencies increase alignment, however frequency appears to have a larger impact on alignment. The effect of CNT length on alignment is then explored, and it is found that alignment is a strong function of CNT length, and major benefits in terms of alignment are achieved above 1.5 μm. Finally, the relationship between concentration, exposure, and resulting film density are explored, and it is found the cavity concentration has a greater impact on the resulting density but shows diminishing returns at high concentrations. It is demonstrated that repeating multiple depositions on the same substrate is another route to increase alignment.

Table of Contents

1 Introduction

Carbon nanotubes (CNTs) are at the forefront of materials science research, yielding exceptional mechanical, thermal, and electrical properties that hold promise in a variety of fields such as energy, medicine, electronics, and aerospace [1-3]. Their unique one-dimensional structure, built from a cylindrical monolayer (1 atom thick) sheet of graphene, allows their electrical properties to be tuned to behave as semiconductors by manipulating the "roll-up" direction, or chiral vector [4]. It is for this reason, along with their exceptional ballistic charge transport properties, that CNTs are being explored for applications in transistors.

Carbon nanotube field effect transistors (CNFETs) have the potential to improve the performance and efficiency of semiconducting electronic devices. Logic devices constructed from highly aligned and densely packed arrays of CNTs will outperform similar Silicon based devices by 5 to 20 times in charge transport, efficiency and switching speed. [5-8]. The excellent properties of CNFETs can only be realized with densely packed, highly regular aligned arrays of nanotube films that are deposited on a substrate upon which FETs can be constructed. Several solution-based approaches have successfully created these nanotube arrays, including shear alignment [9], evaporative self-assembly [10], directed evaporation [11,12], DNA directed assembly [13], dimension-limited self-alignment [14], as well as the Langmuir Blodgett and Schaffer methods [10,15].

While all these methods show promise, significant advances in processing methods and technology are necessary to manufacture the high-quality arrays of CNTs demanded by CNTFETs. The present work aims to better understand, improve, and expand upon solution-

based alignment methods in regard to cost, ease of use, repeatability, and scalability. The present work is organized into three sections. First in section 2.0, the methods used to prepare the substrates is outlined, then the imaging and data collection techniques used to measure alignment and packing density are explained. Characterizing and quantifying alignment and packing density on a large scale is tedious and time consuming, and two methods based on polarized optical microscopy are presented which help to analyze large (millimeter scale) areas of CNT films quickly.

Section 3.0 focuses on improvements to the Tangential Flow Induced Self Assembly (TaFISA) deposition process developed by Jinkins [16]. First, improvements to the physical deposition apparatus are described, then several results are explored concerning the effects of ink flow rate and substrate lift rate on deposition quality, as well as efforts to achieve near full wafer coverage. Finally, challenges facing the scaling of TaFISA, mainly the issue of pooling and sinking of the CNT ink, is explored and remedied.

In section 4.0, a novel method based on substrate-wide confined shear alignment [9] is introduced and the deposition apparatus explained. Applying fluid shear to solution of CNT ink is a known method to induce alignment with the flow direction. The method presented here, called Oscillating Shear induced Alignment (OSA), involves oscillating a substrate with sinusoidal motion within a cavity of CNT ink, producing bi-directional oscillating shear which acts to align CNTs. Results concerning relationships between frequency, amplitude, CNT length, concentration, and exposure time and the variables of interest, mainly degree of alignment and packing density, are discussed and the potential for future work is presented.

2 Materials and Methods

2.1 Substrate Preparation

In order to fabricate electronic devices exploiting the exceptional characteristics of single walled, semiconducting carbon nanotubes (CNTs), they must be deposited on a high quality, semiconducting substrate on which the device can be built. For the experiments described here, single crystal, p-type, SiO_2 wafer with thermal oxide thickness ranging from 90-120nm is used. This substrate has proven to yield high device performance and a thin thermal oxide layer allows for clear imaging with high contrast when compared to a wafer with a thicker thermal oxide. All substrates are received from University Wafer in 50mm or 200mm diameter. In many cases, the substrate is cleaved into smaller pieces for smaller scale testing. Cleaving is done by scribing a small line in the direction of the cut and using a specialized hand tool to cleave it along the desired line.

Often experiments require surface treatments to engineer the interaction and deposition with CNT solutions. For the experiments described here, this includes exposure in an ultraviolet light / Ozone (UV-O_3) cleaner. The ozone radicals bond to any organic residue on the surface of the substrate, and can be easily removed after rinsing in DI water, producing a near-atomically clean surface [17]. For experiments involving deposition of a liquid crystal onto a substrate, the contact angle of the substrate must be controlled to ensure a high-quality deposition. This always begins with a UV-O_3 treatment to clean the surface and bring the contact angle to 0 degrees. After this, the sample is exposed to hexamethyl-disilazane (HMDS), either in the vapor or liquid form. This builds a self-assembled monolayer to the surface, and by varying exposure time, the contact angle can be controlled.

2.2 Imaging Techniques

Analyzing the surface of the substrate after deposition process requires several imaging techniques to fully characterize the density, alignment, and uniformity of the deposited Carbon Nanotubes (CNTs). These images can be analyzed qualitatively without much post processing, or with the help of computer programs images can be characterized quantitatively for a more rigorous comparison. This section provides an overview of the imaging techniques used to characterize the films of deposited CNTs.

2.2.1 Scanning Electron Microscopy (SEM) –

One of the most useful tools for imaging individual carbon nanotubes at high magnification is the scanning electron microscope. In SEM, the sample is placed in vacuum and a focused beam of electrons is targeted at the sample. Electrons are then ejected from the surface and measured by several detectors surrounding the sample. SEM allows for imaging of small features at high magnification (100x – 50,000x). Viewing individual CNTs requires high magnifications (> 5000x), resulting in a tradeoff between imaging area and resolution.

Three similar SEMs were used throughout the subsequent experiments and analysis, provided by the University of Wisconsin – Madison's Nanoscale Imaging and Analysis Center. Listed in order of most to least frequently used, they are the LEO 1550VP, Zeiss Gemini450, and Zeiss LEO 1530.

2.2.2 Atomic Force Microscopy (AFM) –

AFM allows for a more thorough analysis of the substrate surface, with quantitative information on surface height and roughness. AFM utilizes a small, cantilevered tip which

oscillates at high frequency and physically taps the surface of the sample. This signal is then converted to a physical measurement of the surface. AFM allows for high magnification measurements of the surface (> 5000x) to visualize the surface morphology. Often it is of interest to deposit only a single layer (monolayer) of CNTs on the surface, as opposed to several layers on top of one another which can often be difficult to detect on SEM. With AFM, valuable information about stacked layers of CNTs can be measured.

2.2.3 Polarized Optical Microscopy (POM) –

Polarized optical microscopy utilizes a simple optical microscope and polarized light to exploit unique optical properties of the sample surface. Light from a source is polarized in a single plane before reaching the surface, where it is either transmitted or reflected from the surface, where the sample can alter the direction of polarization of the light. This reflected or transmitted light is then passed though another polarizer (an analyzer) into the eyepiece or camera. Based on the spatial orientation of the sample with respect to the polarizers, differences in intensity and color can be seen on the resulting image [18].

POM of CNT films exploits the birefringent properties of densely packed, well-aligned films of rod-like nanoparticles, which display a birefringent property when exposed to polarized light [19]. This means incident light is split into two rays, (ordinary and extraordinary) which differ from the incident light polarization angle by an angle determined by the alignment direction and optical properties of the sample. Depending on the configuration of the polarizer, analyzer, and sample, the image can be adjusted to increase contrast in areas where there is high density and alignment to give a sense of alignment on a large scale (mm) as opposed to on a micro (um) scale. This technique yields information on alignment, density, and uniformity. Put

simply, a region that appears either very bright or very dark (depending on the position of the analyzer) may indicate good alignment and high density, while a region that isn't affected by the analyzer angle would indicate very low density and/or poor alignment.

2.3 Image Processing/Analysis

Raw images from the SEM, AFM, and POM can be used qualitatively without much post processing. To better guide the experimentation process, computational methods are used to extract quantitative information on alignment, density, and uniformity of the sample. This section describes the techniques used to extract that data efficiently.

2.3.1 Rotating Polarizer Analysis

The birefringent property of densely packed, aligned rod-like nanoparticles can be further exploited by measuring intensity of a received signal through cross polarized light as a function of polarization angle. In many instruments it is common for the crossed polarizers to rotate about a fixed location above a sample, but these instruments are often much more expensive that those with fixed optics.

The same effect can be achieved by rotating the sample under fixed polarizers, with the drawback of having to pay great attention to centering the rotation axis about the center of the image. An aluminum adapter was fabricated to accept a Thor Labs rotating stage, and a small locating tool was turned on the lathe, making it easy to attach and remove from the optical microscope. Small steel clips were also fabricated with the waterjet for holding the sample in place during imaging.

During operation, images are taken through a range of 180° at increments of 5 or 10 degrees. In MATLAB, each image is rotated back by its respective rotation angle, ensuring they are aligned with one another. Next, each image is divided into a grid of subregions with dimensions (100x100um), and the intensity of each region, measured at each pixel, is averaged. This way, subregion intensity is measured as a function of the polarization angle. Intensity is correlated with regions of high density, alignment, and uniformity. By assuming a dominating direction of alignment, in this case along the horizontal axis, intensity will peak when the polarization angle is oriented at 45º to the horizontal. This way, the angle of alignment can be determined by measuring the location of peak intensity of each subregion. A map of the dominant averaged intensity is then overlayed on the original image. Figure 1 shows several images taken at different rotation angles and corrected to maintain consistent orientation.

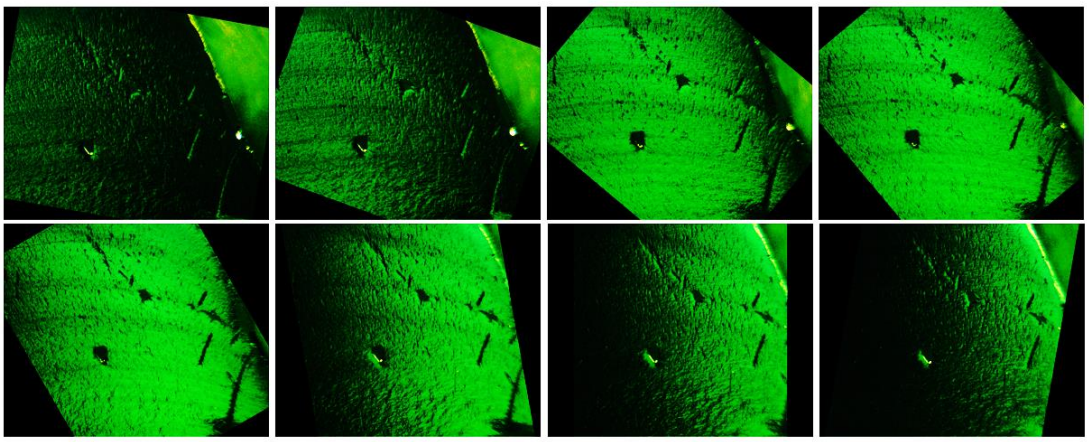

Figure 1: Images taken at the trailing edge of the wafer at varying sample rotation angles. Alignment tends to follow the curved lines

From inspection it can be seen that different regions along the horizontal become more intense at different rotation (polarization) angles, creating a “wave” of high intensity that moves from left to right across the sample. The intensity as a function of position is displayed on the left

in figure 2 below, where each curve represents a region bounded in red in the right side of figure 2. Each region peaks at a different position and has a different maximum intensity. The relative position shift indicates changes in alignment direction while the difference in intensity indicates either a change in CNT density or degree of alignment, where a very densely packed and highly aligned region would be the highest intensity.

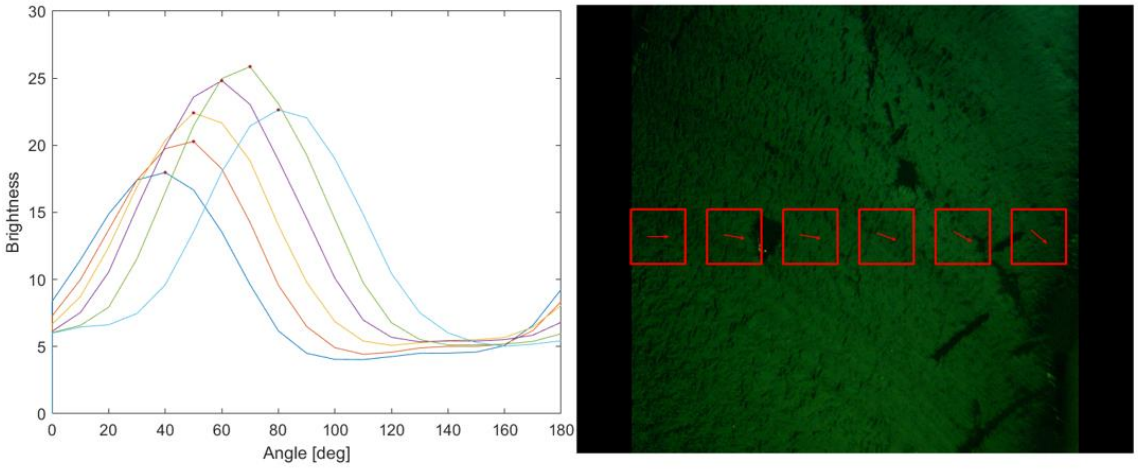

Figure 2: (Left) Image intensity as a function rotation angle for different sub regions. (Right) Resultant alignment map for the sample shown in figure 8 and in the plot to the left

The calculated alignment direction is displayed on the right side of figure 2. It is clear that the arrows follow the streamlines visible on the POM images. Due to the averaging effect of each region, and imperfect positioning of the substrate during rotation, this method is not incredibly accurate, but rather gives a fast and easy method to generate alignment maps of large regions without the need for high magnification SEM or AFM imaging.

2.3.2 Intensity Map Analysis

A single polarized optical microscope image, with the polarizer and analyzer adjusted to show high contrast in the film, can provide useful information about the image intensity as a

function of position. The size, periodicity, and relative intensity of the individual regions are used to quantify the density, alignment, and uniformity of the film on a millimeter scale. A typical sample image is shown in figure 3 for analysis.

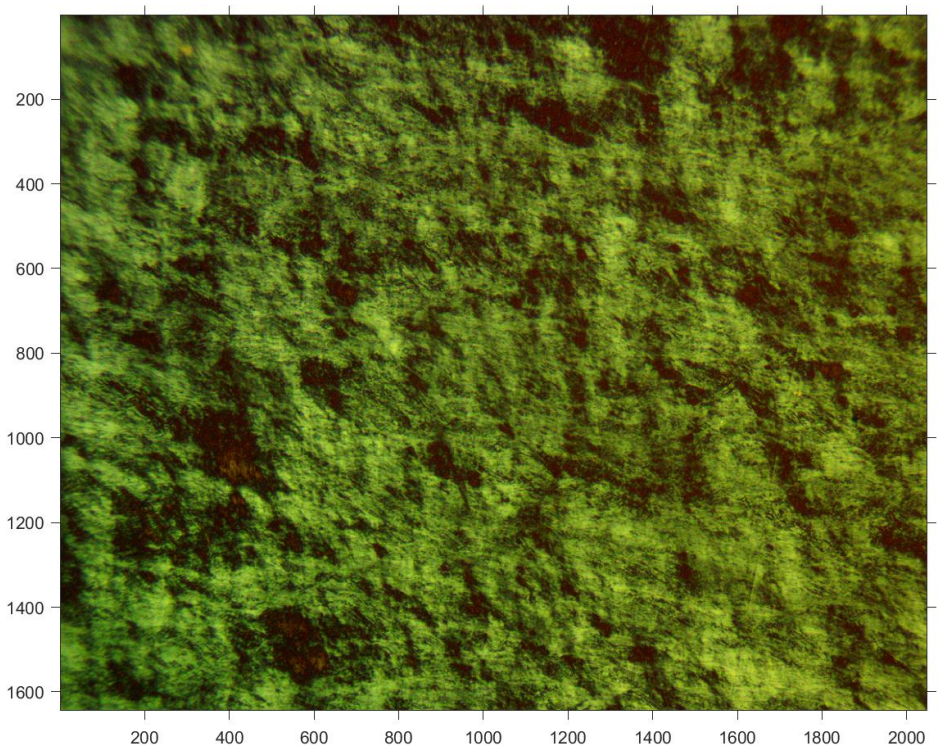

Figure 3: Polarized Optical Microscopy Image of a CNT film on a SiO2 substrate produced with TaFISA. Axes are in units of pixels.

Prior to analysis, the image is discretized into a grid of "sub-images", each of which is a collection of several pixels, in this case, 3x3 pixels. An average intensity value is obtained for each sub-image along a line, usually taken parallel to the flow direction. This can be repeated to create a map of the intensity across the entire image but is visualized more easily when observing the intensity across a single line of sub-images. To account for the intensity bias of the microscope, the input image is blurred to reduce noise, and the difference in intensity of the

averaged and raw image is plotted as the quantitative metric. Figure 4 shows the image after averaging with a large window.

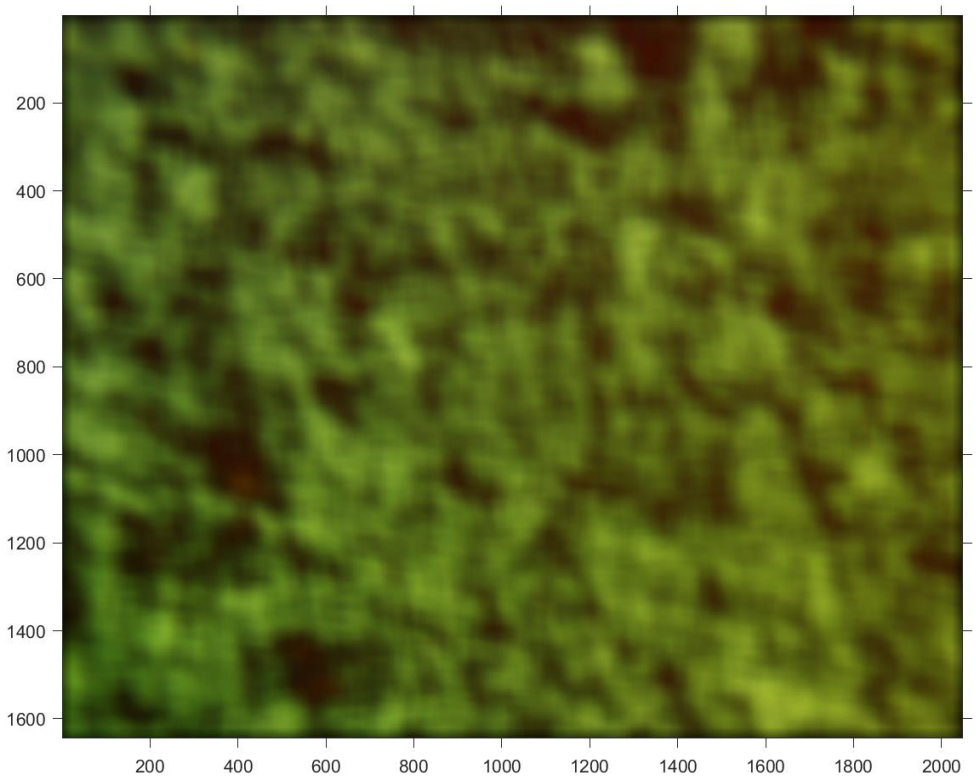

Figure 4: POM image of TaFISA film with averaging applied

This method of averaging was shown to smooth the resulting intensity map, eliminate edge artifacts, and reduce noise. It is worth noting that for large features, this averaging technique will reduce the resulting signal for large regions but will exaggerate the effect seen near the edge of significant intensity changes. This effect can be seen in figure 5, where 2 large peaks are seen around the dark region between 0.35 and 0.7 mm, but the area between them returns close to 0. This method is ideal for analyzing small local features, not features with a size comparable to the averaging window. The resulting intensity map taken at y = 1050 is shown in figure XX.

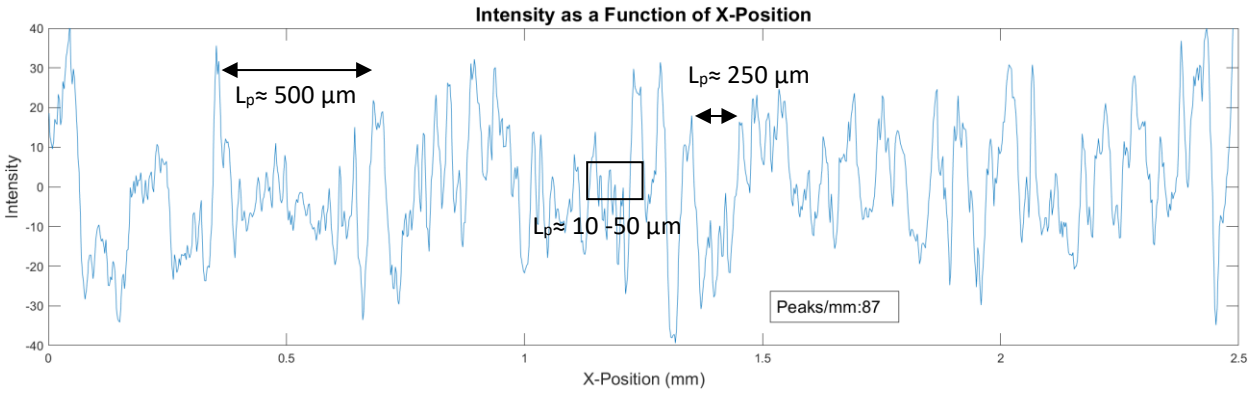

Figure 5: Intensity versus x-position along the horizontal direction at y= 1050.

From figure 5 it is clear the topography of the sample is not very uniform. There are many jagged peaks with small amplitudes, and fewer large amplitude peaks with a larger separation. There is a wide range of peak-peak distances over this range, from 10 – 500 µm. This suggests that there may be some large regions with a dominant alignment direction, within which there exist smaller regions which change direction more frequently.

In order to confirm this analysis, several SEM images are taken in the general area of the POM image shown in figures 4 and 5. Figure 6 shows these SEM images with the local regions of uniform alignment direction highlighted in green, with their associated approximate dimensions labeled. At this scale, the size of the locally aligned regions falls within the expected range suggested by the POM intensity map, indicating this method provides accurate and valuable information about the size and frequency of the locally aligned regions of CNTs.

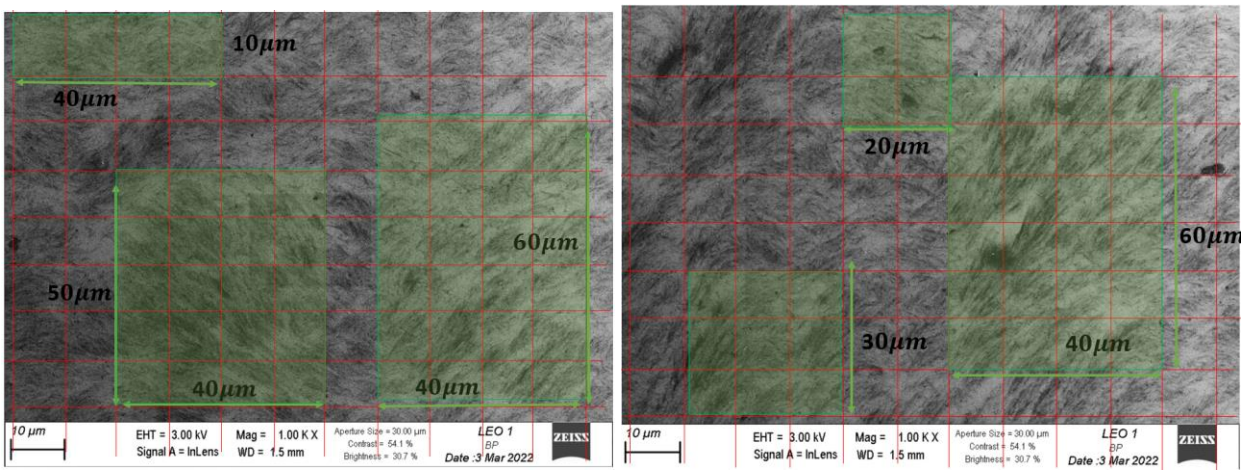

Figure 6: Selected SEM images from a TaFISA film. Regions of local alignment are highlighted in green with associated dimensions labeled

While the above analysis generally confirms that this method is able to resolve the size and frequency of the locally aligned groups of CNTs, a more rigorous analysis is desired to link a given region's alignment, direction, and density to an intensity signal. In the following analysis, a TaFISA sample is patterned using electron beam lithography to create a map that allows a region as small as 10 μm^2 to be located on both POM and SEM.

Figure 7 shows a POM image of a gold pattern laid over a film deposited using TaFISA. This particular film was chosen because it is not very uniform and has frequent changes in alignment direction that can be detected using POM intensity analysis. The entire bounding box is 100 µm, while each of the 8 labeled squares is 10 µm.

Figure 7: POM Image of TaFISA film with gold pattern overlaid

Evidently there are three major distinct colors identifiable in figure 7; green, yellow, and black. From the colors alone, it is not possible to identify a direction of alignment. However, when paired with an SEM image of the same region, specific colors and intensity can be inferred to share a common alignment direction for a given polarization angle. It is also worth noting that the bright / dark regions are dependent on the polarization angle of the microscope's polarizer. A different polarization angle would highlight different common regions and thus different alignment directions.

Figure 8 shows three SEM images of selected regions A, C, and H from figure 7. These images have been traced to highlight the dominant alignment direction and the regions that

correspond to a common alignment. Specific angles are not measured or quantified, but rather large-scale changes in direction are highlighted here. In this analysis, the dominant alignment direction is in the horizontal direction, so the two regions are approximately split into those that have a positive angle (yellow) and a negative angle (blue). Regions that don't have a strong apparent alignment direction are left unmarked.

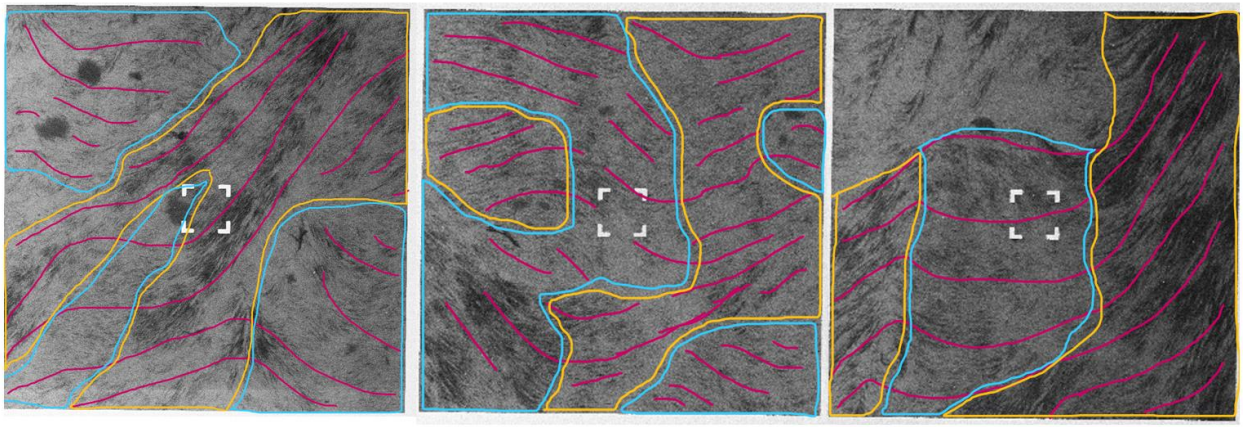

Figure 8: SEM images of regions A, C, and H labeled in figure 7

Comparing figures 7 and 8, it is clear that the regions highlighted in yellow, with a positive alignment direction approximately match the yellow regions in the POM image. Conversely the blue regions with a negative alignment direction correspond to the green regions in the POM image. By inspection, the dense, dark regions in the SEM images with a high concentration of CNTs correspond to much more intense regions in the POM image, as more light is refracted from these regions. In the POM images, the dark regions appear to correspond to areas with low density and without a strong dominant alignment direction.

Region A is cropped, and a similar intensity analysis as described above is applied. Figure 9 shows region A with a horizontal line across the scan direction, with the corresponding

intensity plot as a function of x-position below. The edge regions are cropped to avoid artifacts from the edge of the image.

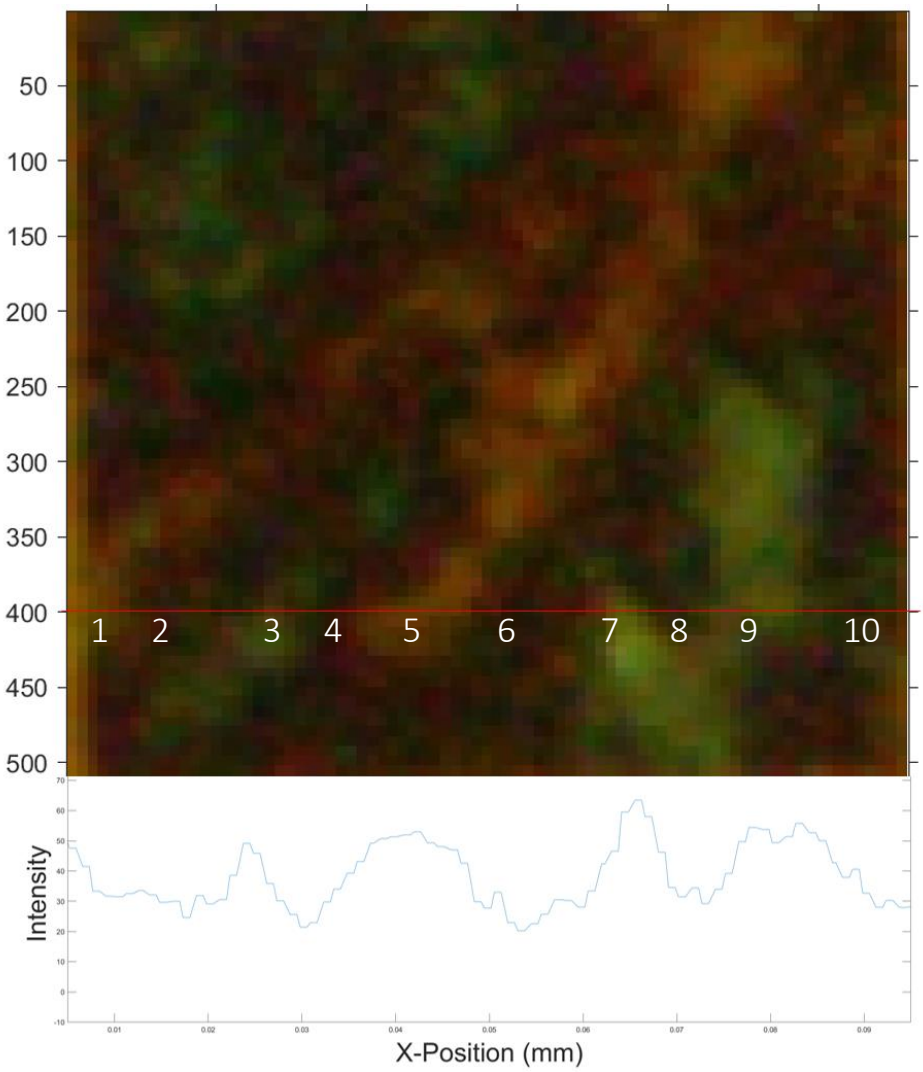

Figure 9: Region A with corresponding intensity plot

Following the horizontal line in figure 9 and counting yellow, green, and black areas yields 10 distinct regions, each indicated by either a peak or a trough on the intensity map. Dark regions, or troughs in the plot, correspond to areas where direction changes, or where there is an interface between the yellow and blue regions outlined in figure 8. This makes sense given the

SEM image of A identifies 4 locations of changing alignment direction, where different regions meet. This implies 4-5 regions of uniform alignment should exist. Inspection of figure XX suggests there are 4-5 distinct regions, confirming the analysis is generally accurate. Although this this analysis is imperfect, it gives a very fast and reasonable estimate for the uniformity of a CNT film.

The method presented here thus proves useful in identifying the frequency and size, and relative density of regions with a common alignment direction in a CNT film. More work is needed to better quantify and measure the alignment direction and density, and correlate these with intensity and frequency, but this work provides a sound foundation for the validity of using pixel intensity to measure alignment in CNT films.

3 Scaling and Engineering Tangential Flow Interfacial Self-Assembly

3.1 Background

Tangential Flow Interfacial Self-Assembly (TaFISA) is a novel method that utilizes liquid crystal formation at a liquid-liquid interface to align two-dimensional arrays of CNTs [16]. Scaling up the deposition area and improving the consistency of this technique is the focus of this chapter. A simplified schematic of TaFISA is shown in Figure 10.

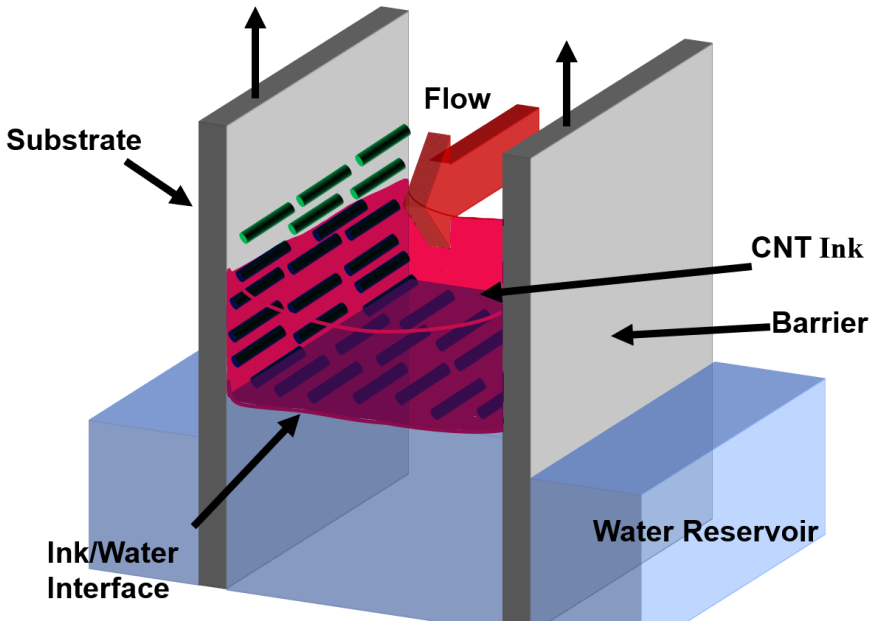

Figure 10: Simplified TaFISA Schematic

The process utilizes a thin channel created between two parallel substrates that is partially submerged in a water reservoir. A needle inserted into the channel delivers a solvent with dispersed carbon nanotubes (referred to as CNT ink) that flows on top of the water. As the CNT ink is injected, surface tension interactions between the water and the ink leads to the formation of a 2D nematic liquid crystal at the solvent-water interface. Nanotubes migrate from the bulk solvent (shown in red in figure 10) to the water-solvent interface. This liquid crystal confines the

nanotubes into densely packed, locally aligned arrays. With the addition of flow through the channel, viscous shear at the channel walls acts to align the CNT groups with the flow direction, creating a globally aligned nanotube film at the interface. As the substrates are lifted from the reservoir, the film is deposited onto the substrate at the ink/water interface [16].

The foundational work on TaFISA demonstrates densely packed, highly aligned arrays of CNTs primarily on relatively small substrates (< 3 cm). Although experiments were demonstrated on larger substrates (up to 10 cm), depositions proved to be more consistent and robust on smaller scales. The work in this chapter describes the efforts made to improve the deposition process, increase repeatability, and better understand the interface behavior, as well as to scale the process up to achieve full wafer coverage on a 2.5” wafer.

3.2 Physical improvements

Several iterations of the experimental apparatus were designed and fabricated, but for simplicity, only the most recent, and best performing apparatus is described in this section.

Barrier Retaining Fixture

One of the most significant improvements to the TaFISA system is the inclusion of glass barriers onto which the target substrate is secured. In the classic configuration, the substrates themselves act as the barriers. Using larger glass plates as the barriers benefits the process in three ways; (1) Allows for *in situ* monitoring of the interface during the deposition process, (2) allows use of a wide range of wafer sizes and shapes, and (3) provides space for the flow to develop and exit the channel without disturbing the deposition near the wafer. Figure 11 shows the experimental setup with the interface visible through the glass. Note the needle positioning fixture (left), 3D-printed plate fixture (upper middle), and the aluminum and glass plates (center).

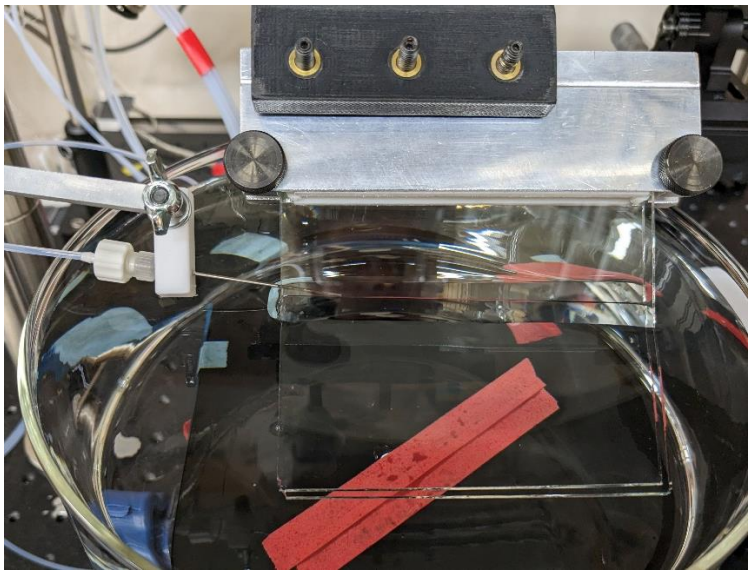

Figure 11: TaFISA Experimental Deposition Apparatus

A two-part aluminum fixture was designed and fabricated to hold the glass plates vertically from the linear stage which lowers and raises them from the trough. Between the aluminum and glass is a PTFE spacer designed to maintain a consistent spacing between the plates. The glass plates, as well as the PTFE spacer can be removed quickly and easily by loosening two thumb screws between experiments. This way, a large quantity of glass plates can be cleaned and prepared in a batch and swapped quickly for efficient depositions. Various PTFE spacers can be used to engineer the channel geometry. For example, section 3.4 explains how a small taper to the channel improves flow stability. Different combinations of PTFE spacers can easily be used to achieve the desired taper.

The external surfaces of the aluminum components have been machined with a small groove which accepts a spring-loaded ball-plunger. Four of these ball plungers are threaded into a rigid 3D printed fixture which attaches to the linear stage. With this addition, the aluminum fixture holding the plates can be removed from the stage with minimal effort, without the need

for tools, and replaced without sacrificing positional consistency. This makes the deposition process more efficient, simpler, and more easily repeatable for the operator.

Needle Positioning Fixture

One of the most critical variables in the TaFISA process is the needle positioning in the channel. In order to achieve good flow, the needle must be centered exactly in the center of the channel, held at a consistent 10–15º angle, and must be able to move perpendicular to the barriers. Between trials, the needle is often removed and cleaned, so it is important that the needle can be removed and inserted into this fixture without the need for re-adjustment.

Several methods were explored to achieve this, but the most effective solution is shown in figure 12. Here, a combination of angled fixtures, linear stages, and custom waterjet-cut aluminum components suspend a small PTFE block which holds the needle in place. The PTFE block can pivot to alter the needle angle and lock in place. The linear stages are angled such that the needle can be moved in the direction of the width of the channel and along the height.

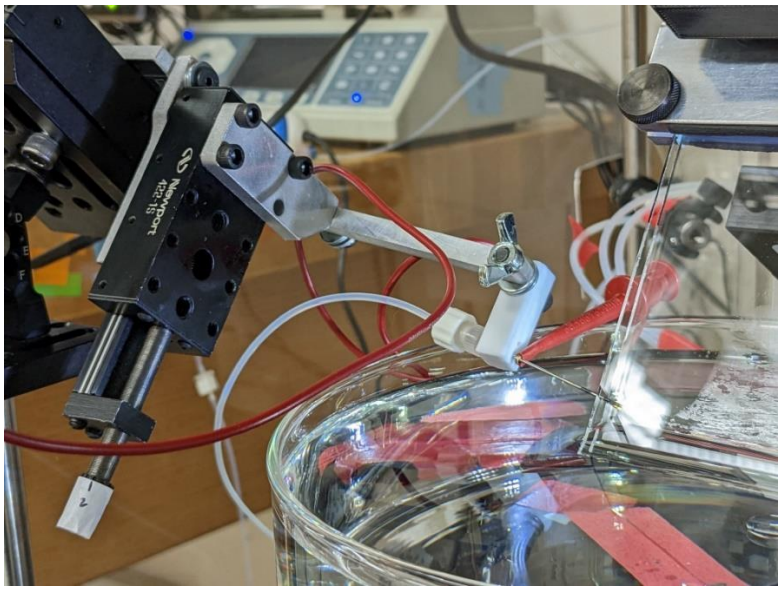

Figure 12: TaFISA needle positioning fixture

The “horizontal” needle position can be centered by performing a “touch-off” on either glass plate. The needle can then be moved by half the width of the channel using the precision linear stage. The vertical needle position is also critical to the TaFISA process, and since the water level often changes slightly between experiments, a standard reference is necessary to achieve repeatable placement. The simplest method is to use the water itself. Using a Keithley conductivity probe, with one end attached to the stainless-steel needle and the other submerged in the water trough, the needle can slowly be lowered until it touches the water surface, after which the height can be adjusted relative to the water surface. A probe with very high sensitivity is necessary, as the water used in these experiments is of high purity and has a resistance of ~14 MΩ.

With the improvements explained here, the needle position relative to the water surface and channel walls can be completely controlled, a critical step in creating a robust and deposition apparatus.

Constant Water Level Device

In classic TaFISA, the substrates are the only portion of the apparatus submerged in the water. This fact, along with the smaller deposition areas associated with classic TaFISA, means a very small volume of water is displaced by the substrates. With the addition of thicker and larger glass plates as well as larger deposition areas, the amount of water displaced is significant. During a deposition as the plates are removed, the water level in the reservoir drops and often times loses contact with the needle. Given TaFISA’s sensitivity to variables such as needle placement, a method a maintaining the water level in the reservoir was required.

A constant water leveling device, a modified siphon, was fabricated from an acrylic tube, rubber stoppers, along with glass and copper tubing according to the design described in [20]. Figure 13 shows the water leveling device and its components. Once the siphon is established between the reservoir and the device, a steady supply of water enters through the top and continues to drain as long as the water level in the reservoir remains constant. As the plates are inserted or removed, the water level in the trough rises or falls, and a pressure difference exists between the reservoir and the siphon, which can either remove water or supply water to the reservoir. This device provides a passive solution where small changes in water level are adjusted for, effectively maintaining a constant water level throughout the deposition process.

Figure 13: TaFISA water leveling siphon

3.3 Results and Observations

3.3.1 Effect of flow rate and substrate lift rate on film quality

The delicate process occurring at the three-phase contact line in TaFISA is sensitive to many independent variables. The CNT ink flow rate and the substrate lift rate are suspected to be particularly important in the liquid-liquid interface dynamics, the formation of a liquid crystal at the interface, and the transfer of this crystal to the substrate. Evidently it also appears these variables may be coupled, where only a balanced combination of flow rate and lift rate yield the desired results. This section briefly explores the effect of flow rate and substrate lift rate on resulting film quality.

In the classic TaFISA configuration, it was found through experimentation that a flow rate of 4 mL/min, and a substrate lift rate of 40 mm/min yield the most highly aligned, uniform films [16]. The effect of flow rate is studied from 0 to 4 mL/min, and several lift rates are studied, from 7 to 100 mm/min. Several conclusions are made about ink flow rate; For example, alignment improves with increasing flow rate, up to 4 mL/min. Similar results are seen with 8 mL/min, but substantially higher flow rates of 16 mL/min diminishes ordering and introduces more defects [16]. It was proposed that flow instability and turbulence are the explanation for the decreased film quality. This result appears intuitive and is supported by the fact that in this configuration, the flow begins to transition to turbulence at flow rates near (10 - 12 mL/min).

The combined effect of flow rate and lift rate, however, is a unique relationship that has not yet been studied explicitly. Here, an isolated experiment is designed to evaluate the coupled effect of ink flow rate and substrate lift rate. Three flow rates (4, 6, and 8 mL/min) paired with three substrate lift rates (40, 60, and 100 mm/min) are tested for a combined 9 unique conditions.

To minimize the effect of substrate and CNT ink variation, three flow rates were tested on a single substrate in a single run at a fixed lift rate. This way, three separate regions exist on a single substrate with identical surface and ink preparation and can be directly compared. Tests are conducted using a programmable Nexus 3700 syringe pump to deliver a specified volume of ink at a prescribed flow rate with continuous substrate motion. This procedure results in a substrate with three separate 2 cm regions each with a unique combination of substrate lift rate and flow rate.

Figure 14 shows selected images taken along a single line parallel to the flow direction for each combination of lift and flow rate. Figure 15 shows images for 8 mL/min at a substantially higher lift rate of 200 mm/min. Figure 16 shows a plot of image intensity as a function of x-position along the flow direction for the images on the far right in figure 14. This intensity analysis, explained in section 2.2.2, provides quantitative information about the uniformity and periodicity of the bright and dark regions present on POM images of TaFISA samples. Pairing this analysis with SEM images can provide valuable information on the film on a larger (mm) scale.

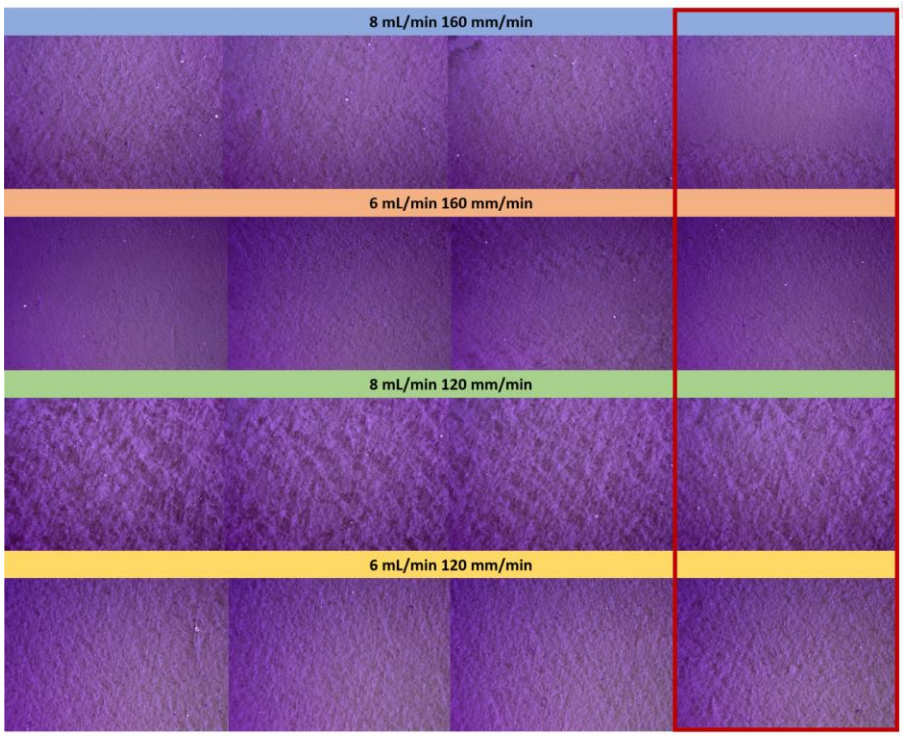

Figure 14: POM images taken along the flow direction for various flow rate and lift rate combinations

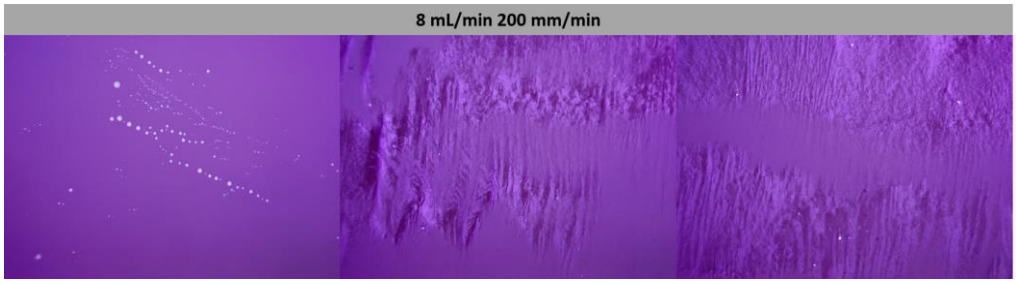

Figure 15: POM images taken along the flow direction for 8 mL/min and 200 mm/min

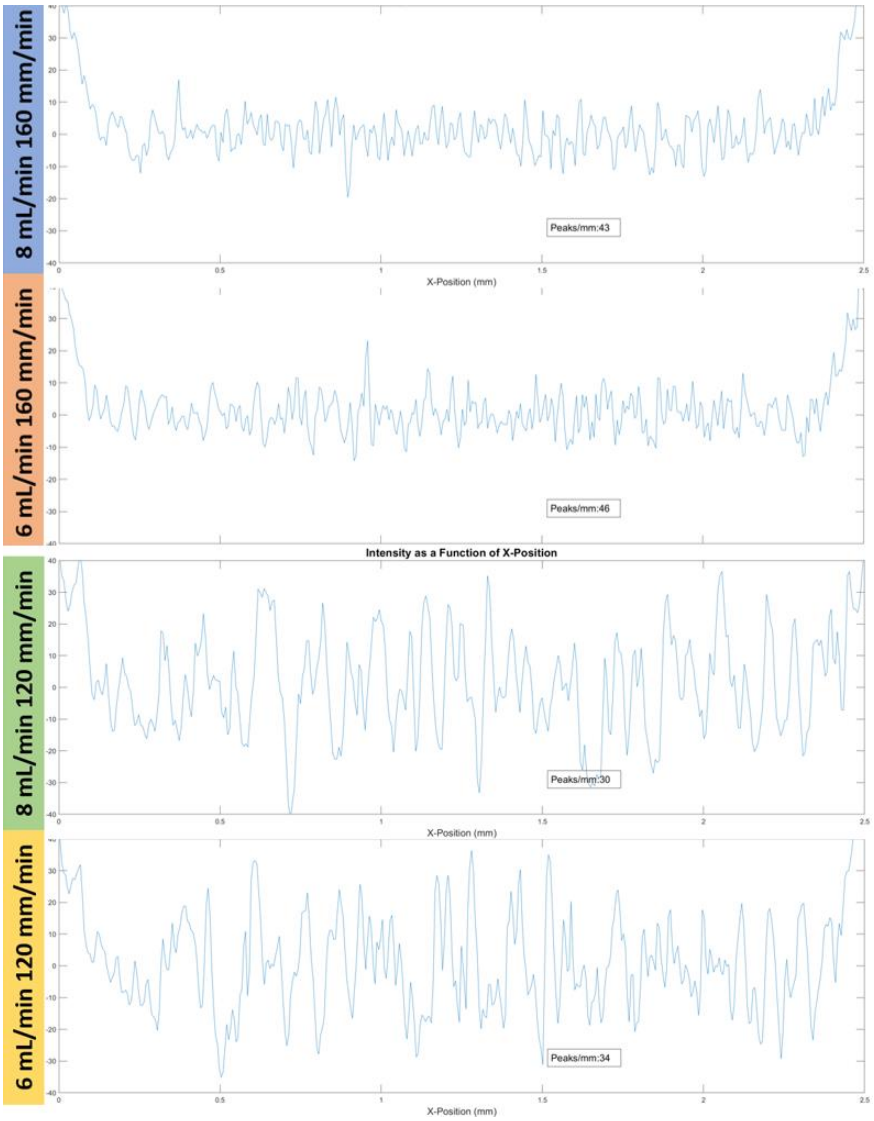

Figure 16: Intensity as a function of x-position for various flow rate and lift rate combinations

From figures 14 and 15, several conclusions can be made. The first is that even small differences in substrate lift rate and ink flow rate have a significant effect on the resulting film quality. While depositions at lift rates of 120 and 160 mm/min produce relatively uniform films, an increase in lift rate to 200 mm/min results in no deposition. One possible reason for this may be the instability, or the stick-slip motion, of the 3-phase contact line. The 3-phase contact line

between the water, chloroform CNT ink, and air must translate smoothly over the substrate in order to deposit an organized film. It can be shown through observation of the interface that high lift rates result in more irregular motion of the 3-phase contact line.

When looking at figure 16, several quantitative values are of interest. The most obvious is the average amplitude of the intensity oscillations. For a lift rate of 160 mm/min, the average amplitude falls within ±10 intensity units for both flow rates. For a lift rate of 120 mm/min, the amplitude increases to ±32 intensity units. This means that there is a greater change in brightness between neighboring regions, meaning that the bright regions are brighter, and the dark regions are darker, relative to one another. Regions of bright and dark are misaligned with each other, and their intensity depends both on degree and direction of alignment (uniformity) as well as packing density. A high amplitude likely means that the regions are more densely packed and/or more well aligned *locally* than a low amplitude counterpart. It is assumed that a consistent low amplitude signal implies that the regions are well aligned globally, and do not change direction significantly. Note that this is only because the intensity value shown on the plot is normalized by the average intensity of the overall image. Excluding this step, a well-aligned film would appear uniform and bright. It is also worth noting here that a low amplitude signal could also result from a sparse and non-uniform film, (which is later confirmed with SEM images). The frequency of oscillations gives information about how often the regions change direction and gives a measure of the global alignment.

With this information, the high amplitude, lower frequency signal of the lower lift rate implies local groups of dense, highly aligned NTs that change direction roughly 32 times every millimeter. The lower amplitude, high frequency signal implies a more uniformly aligned film,

with less drastic changes in alignment, but a higher number of small oscillations, on the order of $45mm^{-1}$.

Evidently it appears from this data that substrate lift rate has a more significant impact on film quality than lift rate. When isolating the effect of lift rate however, it can be argued that a lower flow rate produces a slightly higher number of directional changes. This could be due to the fact that at higher flow rates, there is greater viscous shear which acts to align the liquid crystal with the flow direction.

3.3.2 Demonstration of near full wafer coverage

One of the more promising aspects of the improved TaFISA apparatus is the flexibility in regard to where the needle can be placed relative to the substrate. In classic TaFISA, the target substrate is used as a barrier, so the needle must be placed over the substrate, as shown in figure 17. This restricts the deposition area to only the portion of the substrate that is below and beyond the needle. Additionally, there exists a “developing” region, denoted in yellow where it is suspected the liquid crystal formation is established. In this region (which is found to be roughly 2 cm, depending on process conditions) no film is transferred to the substrate, until it begins to establish with a striped pattern until it becomes uniform. This means in the classic configuration; a significant portion of the target substrate has little to no deposition. The uniform region, colored dark blue, is the high-quality film, and ideally, the entire wafer will be a continuous, uniform film.

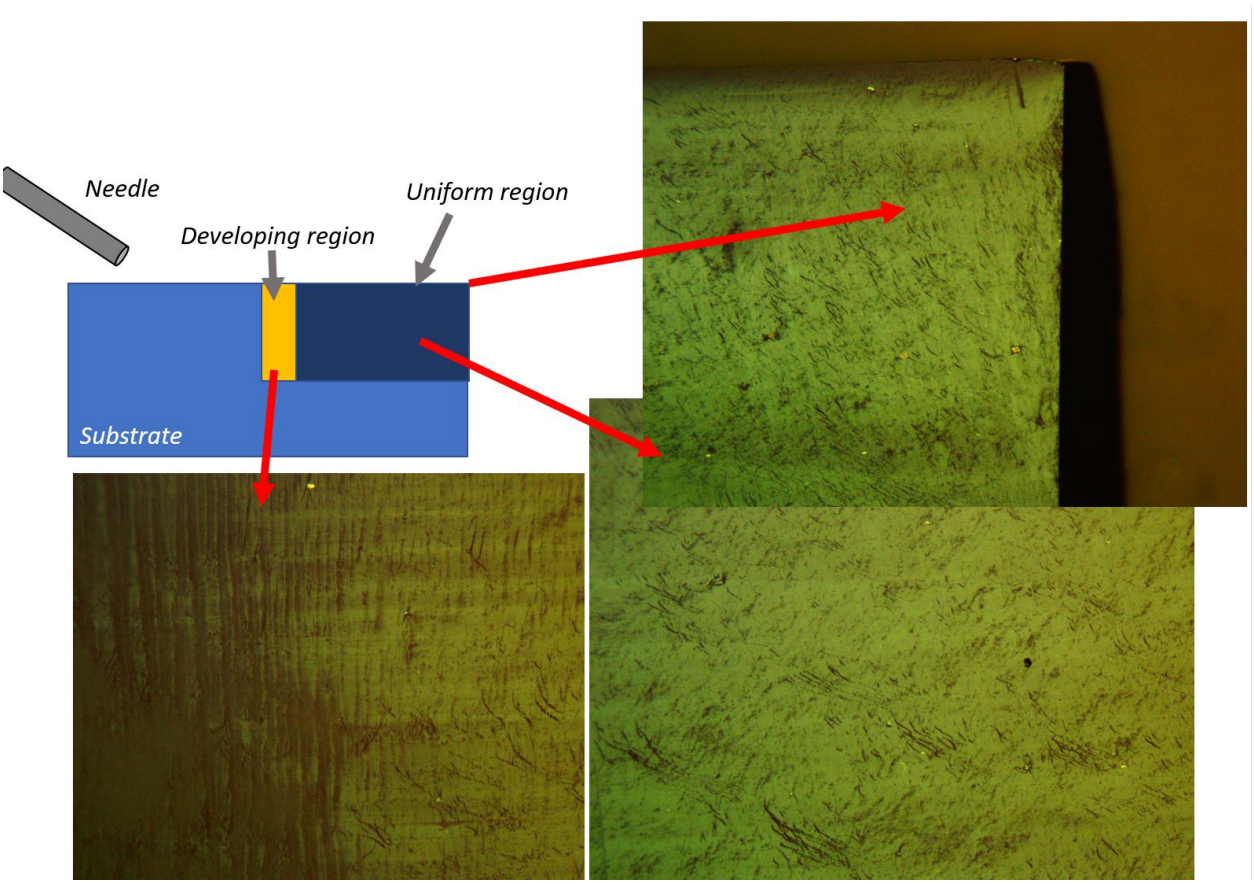

Figure 17: Classic TaFISA deposition configuration and corresponding POM images

The new TaFISA apparatus utilizes a sacrificial barrier onto which the substrate is secured. This way, the needle can be placed within the sacrificial glass barriers, leaving room above and ahead of the substrate where the film can be established with the goal of producing full wafer coverage. A visual is provided in figure 18 to demonstrate the difference in these configurations. It is worth mentioning that full wafer coverage versus partial coverage is a significant step in improving the process, as the entire substrate can be utilized to make devices, rather than only a fraction of the substrate.

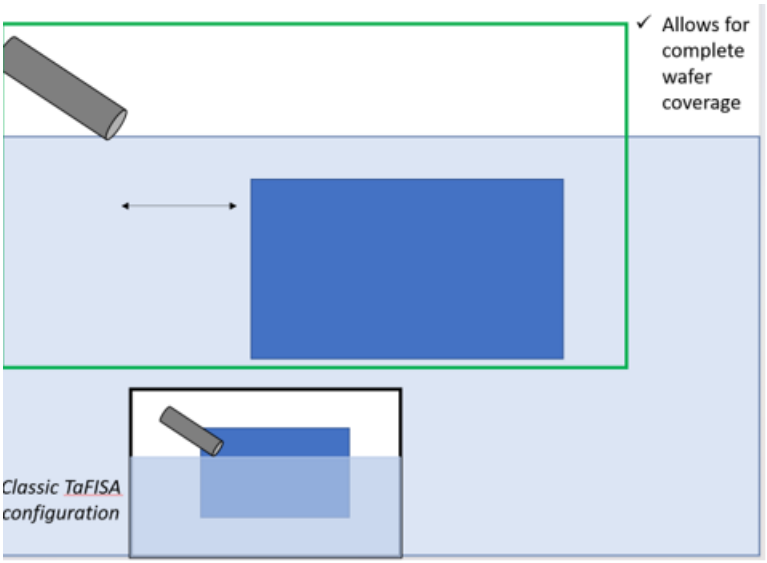

Figure 18: Schematic of needle placement comparison with classic TaFISA (below) and Plate TaFISA (above)

With the current apparatus, it is possible to achieve roughly 90% coverage depending on the substrate size. Figure 19 shows the size and placement of the clamp, a waterjet-cut 0.5 mm thick stainless-steel clip, on a 2” diameter circular wafer. It is clear that any area under or beyond the clamp is negatively affected. Still, this method allows for the highest percentage of coverage demonstrated in TaFISA.

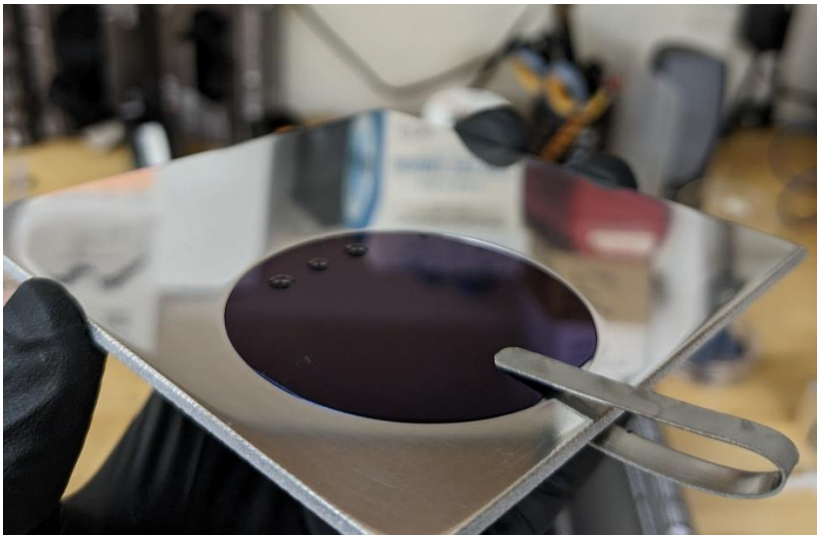

Figure 19: 2" circular wafer clamped on polished aluminum sacrificial barrier

It is worth noting that other methods exist for securing the wafer to the substrate without sacrificing any area, but they were deemed out of the scope of this experiment. The most promising method in an industry setting is most likely utilizing a small hole in the glass barrier under the substrate and applying a negative pressure to secure the wafer. This concept was explored using a venturi tube, and a waterjet-cut piece of glass. By applying a positive pressure at the inlet of the venturi tube, a negative pressure is created near the converging section of the nozzle, which is attached to the hole in the glass. Since the glass and substrate are nearly flat surfaces, the seal created is sufficient, and no gasket material is necessary. The entire fixture can be submerged in water without leaks. In future versions of TaFISA, where 100% wafer coverage is the goal, this method is recommended.

Using a flow rate of 4 mL/min and a substrate lift rate of 40 mm/min, a deposition on a 2 x 4 cm rectangular substrate was carried out with the needle configuration described above. Figure 20 shows a map of the substrate and POM images of the resulting film. Evidently, the film appears very uniform and bright, with minimal dark regions. This indicates that the film is uniformly aligned and dense across the substrate. Images near the top and far edges of the substrate also confirm the film transferred neatly onto the substrate without adverse edge effects. Using the intensity analysis described above, the uniformity can be compared to the samples analyzed in figure 16 of section 3.3.1.

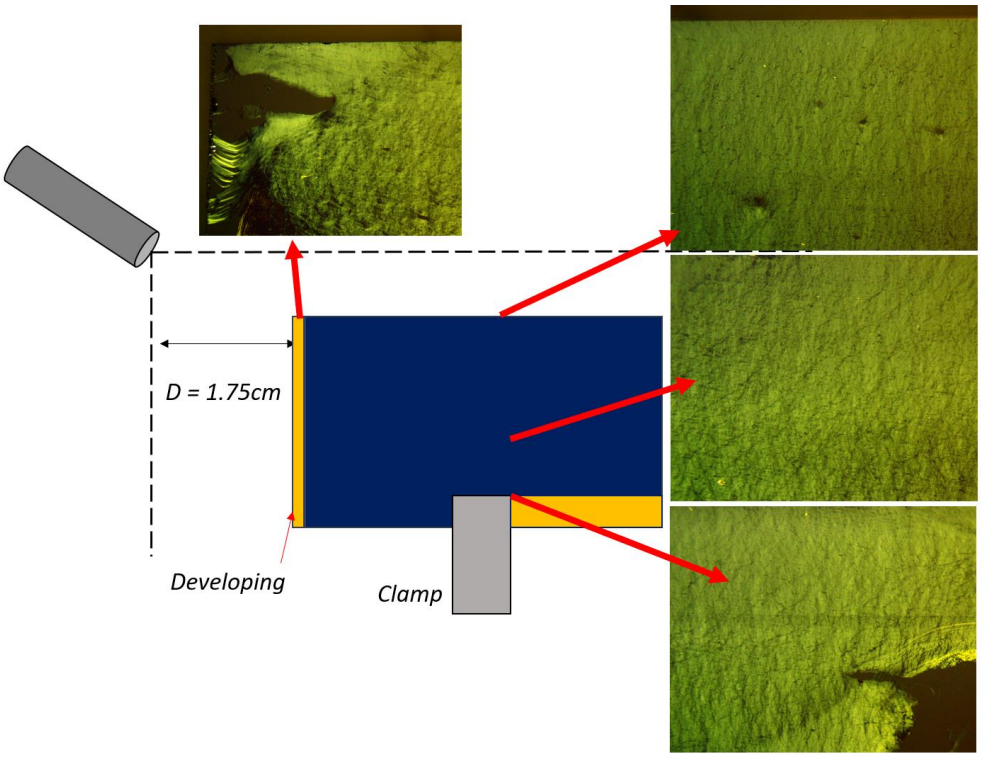

Figure 20: Schematic of needle configuration and wafer coverage, with corresponding POM images

Figure 21 shows the intensity as a function of position, when compared with figure 16, the amplitude is much smaller, indicating a more uniform alignment across the substrate, with fewer large changes in direction. The frequency (peaks / mm) is much higher, indicating that there are many small changes in direction across the substrate, but generally, the alignment has a strong global direction indicated by the small amplitude. The higher frequency signal could also be an artifact due to the method here being sensitive to noise. It is possible in future work that a method to decrease the threshold for a “direction change” be increased to exclude very small changes in direction.

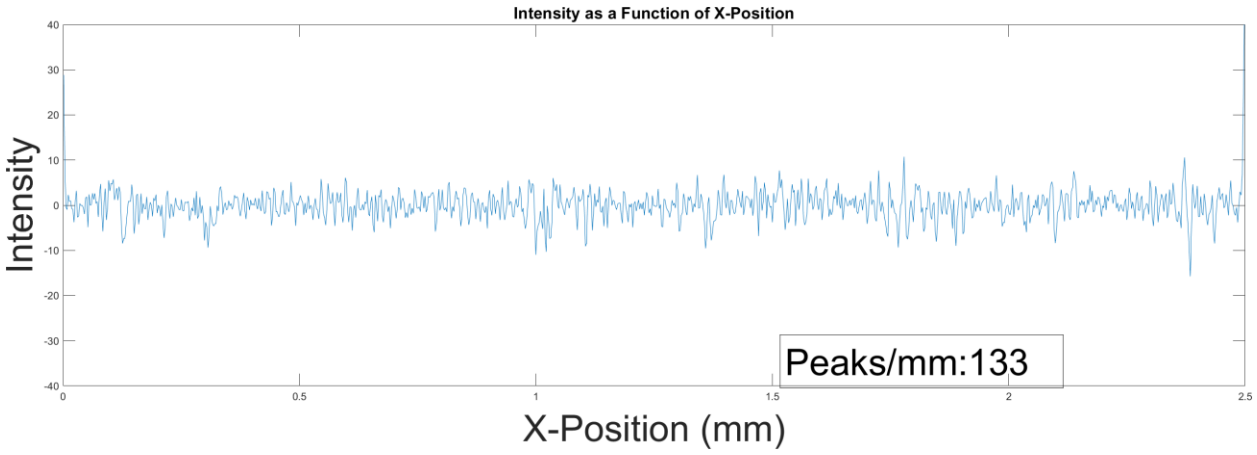

Figure 21: Intensity vs. x-Position of the POM image shown in bottom right of figure 20

The region analyzed in figure 21 is inspected using the SEM in order to confirm the conclusion that the film is uniform and globally aligned with the flow direction. Figure 22 shows SEM images which indicate relatively uniform alignment across the sample. Small "waves" are present, as well as liquid crystal defects, which decrease the uniformity of the film, and may contribute to the high frequency signal shown in figure 21. The directional changes are small however, and the alignment here can be quantified to fall between +/- 15 deg. Counting the number of directional changes in figure 22 on the left yields roughly 10 changes across the image, which is about 100 µm in width. This equates to a change in direction roughly every 10 µm, or about 100 changes in direction every millimeter. Although this is a rough estimate, it adds validity to the "peaks/mm" metric attained from the intensity analysis because it is on the same order of magnitude as the number of direction changes identified in the SEM image.

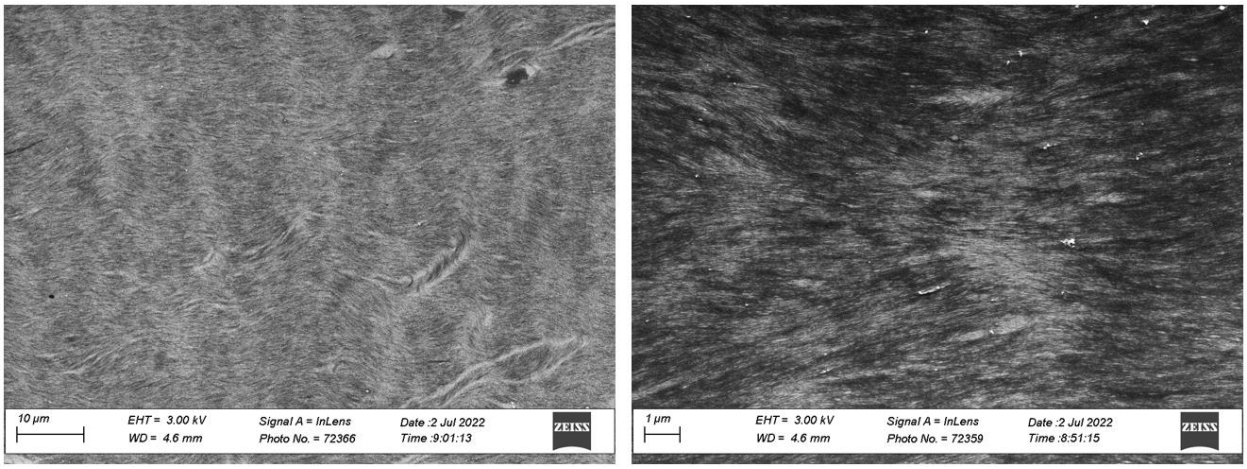

Figure 22: SEM Images demonstrating a uniformly aligned CNT film

Figure 20 also shows an incomplete region in yellow beyond the clamp holding the substrate. This makes sense, because the clamp, while thin (0.5 mm) still disrupts the flow in the channel, and inhibits either the liquid crystal formation, or its transfer to the substrate. A different clamping method, (such as suction mentioned above) would remedy this issue. It is also clear from figure 20 that there is a small developing region near the needle-edge of the substrate. This was assumed to be caused by the needle being placed too close to the substrate. The developing region is roughly 2 cm in length, and in this case the needle was placed roughly 1.75 cm from the substrate edge, which may explain the small region of incomplete film present on the substrate. Still, this is a significant improvement, and suggests full wafer coverage is attainable with minor additions to the apparatus.

3.4 Characterizing and controlling the stability of a dynamic stratified suspended liquid

Section 3.4 is adapted from Prussack, B.A., Foradori, S.M., Droplet formation in dynamic stratified liquid-liquid systems for solution-based deposition methods. *ASME Journal of Fluids Engineering*. (2023). B.A.P and S.M.F performed all experiments, B.A.P drafted the manuscript.

3.4.1 Introduction

The incredible quality of the highly aligned and densely packed films achievable with TaFISA are demonstrated by Jinkins, and in sections 3.3.1 and 3.3.2. Films with alignment within ±6° and packing densities near 100 NT/μm are achievable repeatably on a relatively small scale. While this is a major step in improving CNT film deposition quality, in order for a method such as TaFISA to be adopted by industry, the process must be scalable to larger substrates. In an industry setting, silicon wafers are received in standard sizes that range from 2.5 cm in diameter to 30 cm. The steps to process these wafers are time consuming and expensive, so treating large areas at scale is much more efficient than individually preparing a high number of smaller substrates. After preparation, the large wafers can then be cleaved into smaller sections depending on their application. Thus, it is preferred that TaFISA can be applied to large substrates to take advantage of manufacturing at scale.

Previously, TaFISA was carried out on small sections of substrates, cleaved from full SiO_2 substrates to conserve expensive nanotube ink. Isolated experiments on a 10 x 6 cm substrate demonstrate approximately 60% coverage, or roughly 30 cm^2 where the film is uniform

[16]. While this is an improvement over the small-scale tests, it is preferred to increase percent coverage as well as total film area in order to further demonstrate scalability.

There are many challenges facing the transfer of a large continuous, uniformly aligned liquid crystal film to a substrate, including liquid crystal phenomena, maintaining ordered flow, and controlling stick-slip motion of the three-phase contact line. Perhaps the most detrimental is preventing the pooling and sinking of the dense CNT ink while it is confined within the channel. A large substrate requires a longer channel length which the ink must travel before exiting into the water reservoir. The ink slows due to viscous friction, and eventually collects in a pool within the channel. As this pool grows, it overcomes the supporting surface tension forces and drops through the water interface, disrupting the deposition completely. Typical pooling behavior is shown in the sequence of images in figure 23. Even a single pool can ruin an entire deposition, as once it forms, the ink continues pooling and dropping and the organized flow within the channel is lost. Understanding, modeling, and preventing this pooling behavior is the focus of this section.

Figure 23: Evolution of droplet formation in the TaFISA channel

3.4.2 Experimental Apparatus

The experimental apparatus used to study this effect is shown in figure 24. It differs slightly from the apparatus shown in section 3.2 but is functionally very similar. The apparatus utilizes two aluminum frames which hold removable glass barriers that act as the channel. The

transparent glass plates allow the behavior of the liquids in the channel to be observed during the deposition process. Parameters such as needle insertion height, ink film thickness, and water level variations and vibrations can be observed and measured. The aluminum frame is connected to a linear stage that lifts the fixture from the water trough at a controlled rate. The process is sensitive to the water level height in the channel. Therefore, as the plates are lifted from the trough a water leveling device is used to maintain a constant water level in the trough.

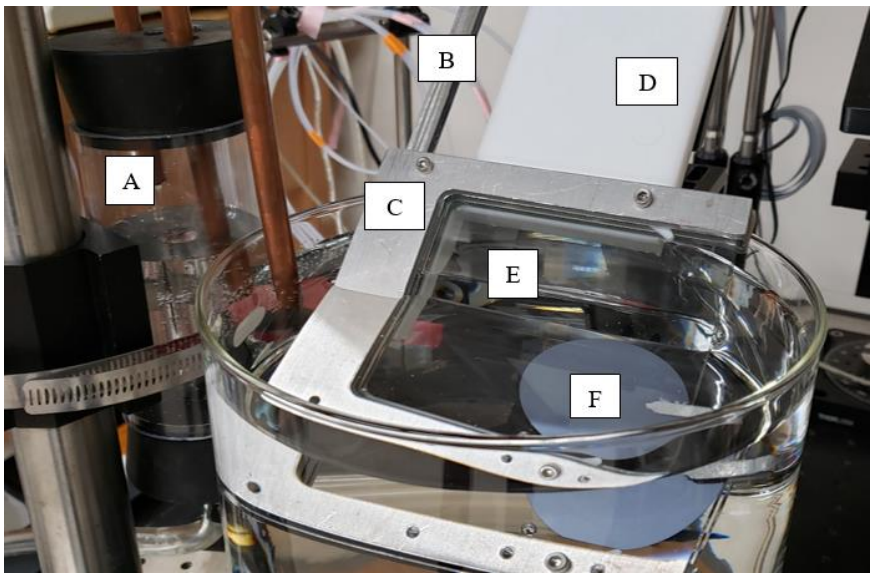

Figure 24: Experimental apparatus. From left to right: (a) the water leveling device, (b) floating stationary post, (c) aluminum plates, (d) linear stage, (e) glass barriers, (f) sacrificial target substrate

The needle that delivers the ink is held in place using an aluminum post fixed relative to the plate motion; a series of holes in the post can be used to position the needle at various angles relative to the water level. The post fits within a small recess between the aluminum plates with the needle positioned between the glass barriers. The post acts as a barrier to prevent backflow of the CNT ink out of the channel, directing all of the ink flow through the channel. The post is mounted to an independent and manually controlled linear stage that allows for accurate control

of the needle height position relative to the water level and ensures that the needle remains stationary as the plate is lifted from the water.

3.4.3 Flow Characteristics

The issue of pooling and sinking ink must be addressed in order to allow an ink flow to be established through the entire length of a long channel in a consistent and controllable manner. To scale TaFISA and other solution-based processing methods to larger wafers, it is important to develop a general understanding of the behavior of the fluids involved (CNT ink and water) within the channel and the impact of various operating parameters on the achievable front distance (i.e., the distance that the CNT ink travels before pooling).

The flow within the channel in TaFISA can be classified as a stratified flow of immiscible liquids between parallel plates. In this case, the lower fluid phase is a deep reservoir of stationary water. The upper fluid is a higher density layer of liquid flowing through the channel; this flow is bounded on three sides but remains open to the atmosphere above. Research on similar stratified gas-liquid and liquid-liquid flow has focused on internal pipe flow, primarily with the less dense fluid on top [21]. The primary focus of these prior studies is the characterization of the interface that separates the two fluids and the prediction of pressure drop and liquid hold-up. Few studies have been done on stratified liquid-liquid flow between parallel plates and those that do exist focus on situations in which the less dense liquid is supported on a higher density subphase. For example, the work by Keulegan [22] focuses on the interface behavior in this situation, specifically the formation of waves and the resulting mixing that occurs as a function of the flow rate. This study shows that the flow velocity, fluid density, and viscosity all play a substantial role in the interface behavior.

Another area of research that is relevant to the pooling and sinking behavior observed during TaFISA is the gravitational stability of liquid lenses that are supported on a liquid subphase. Research in this field primarily focuses on the wetting/spreading behavior of lower density liquid lenses on a higher density subphase, with few studies discussing the opposite case [23,24]. Other studies investigate the stability of water droplets and solid cylinders suspended on a liquid subphase [25,26]. Results from these studies show that interfacial surface tension forces and contact angles play a significant role in the stability of the suspended liquid; however, none of these works address the details of pooling and sinking of the upper fluid. Additionally, this prior work has been carried out on static systems and does not consider the dynamic forces that arise in a flowing situation. To the authors' knowledge, the stability of a dense liquid film flowing over a less dense liquid subphase between parallel plates has not been previously investigated.

This study is divided into an experimental section in which the experimental procedure and data collection process are described. The data are then presented, and some observations are identified in order to motivate the subsequent analysis. The results and discussion section investigates the dominant forces associated with the stratified flow that exists within the channel and identifies relevant dimensionless numbers that are used to define a critical condition where pooling behavior is likely to occur. This critical condition is used in the context of a simple model to develop a correlation for front distance. Finally, the results from the correlation are used to suggest methods for increasing front distances for longer channel widths.

3.4.4 Data collection and analysis

The pooling and sinking behavior of a suspended, high-density liquid supported on a lower-density liquid and flowing in a thin channel is studied using the experimental apparatus developed for TaFISA that is described above and shown schematically in figure 26.

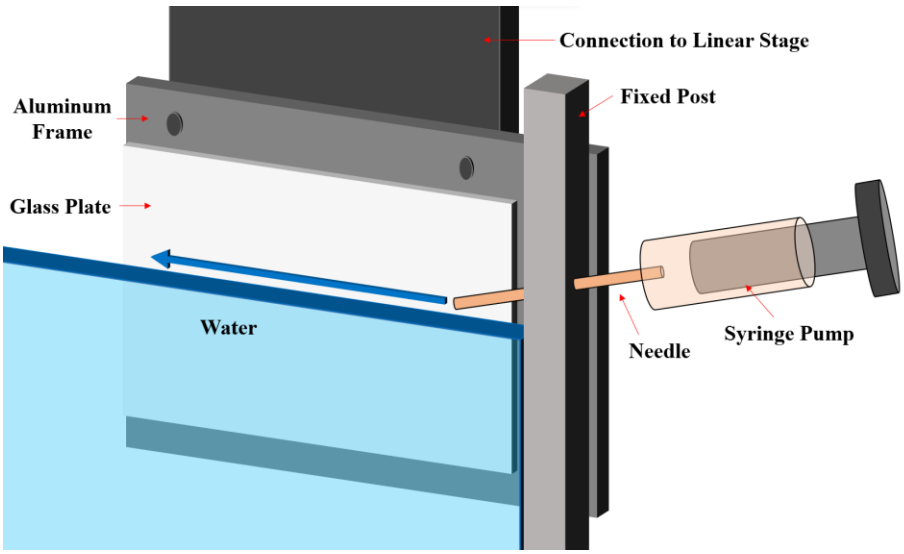

Figure 25: Schematic of experimental apparatus with the near plate and barrier omitted

The channel is created between two 10 cm square glass plates that are separated by spacers that control the channel gap. The glass plates are held in an aluminum frame which is attached to a motorized linear stage. The plates are partially submerged vertically in a trough filled with clean, ~14 MΩ water. The water contact line is visible through the transparent glass plates. The ink (chloroform) is introduced into the channel through a 1 mm inner diameter needle that is held in a post at the entrance of the channel. The needle is held at a 5° angle from the horizontal and centered in the channel. The chloroform flow rate is controlled using a Nexus 3700 syringe pump. The data collection process starts by partially submerging the plates in water, after which the needle height is set using a linear stage to move the post vertically. A flow rate is selected, the syringe pump is activated, and ink flow is initiated. The behavior of the

interface is recorded using a Dino-Lite Basic AM2111 camera. During each test, either the ink front reaches the end of the channel and exits successfully, or the front slows and pools before the exit. In the latter case the front distance (i.e., the distance between the point the ink exits the needle and the point that it pools) is recorded. After each run, the plates are fully removed from the trough with the linear stage and the ink is allowed to evaporate from the plates and the water surface. The plates are then re-inserted, and the process is repeated for the next test.

A scale is attached to the plate to allow the front distance to be measured accurately based on video recorded during the process. The pool typically has a width of roughly 1 cm, and the pooling location is taken to be the center of the pool. Measurements are only recorded for tests during which pooling and sinking occur. For tests where the ink successfully reaches the far end of the channel, a front distance cannot be measured and therefore these trials were not considered in the data collection. Under some conditions, pooling initially occurs a short distance from the needle and the location of pooling subsequently slowly moves towards a maximum value. Under these conditions, the front distance was recorded after the pooling and sinking location has stopped moving.

The front distance as a function of needle height was initially studied to determine how sensitive the process is to this parameter. A needle height of zero corresponds to the bottom edge of the needle just contacting the water surface. Any further movement into the water is taken to be an increase in needle height. Figure 27 shows the front distance as a function of needle height measured at flow rates of 4 mL/min and 6 mL/min for a 1.5 mm plate separation. For a given flow rate, figure 27 shows that the front distance remains constant to within about 0.5 cm regardless of needle height, indicating that the effect of this parameter is relatively insignificant. For the remainder of the data collected, a needle height of 0.75 mm is used. This leaves the

needle partially submerged in water. Above 1.5 mm, the needle is fully submerged which causes the chloroform to sink immediately after exiting the needle.

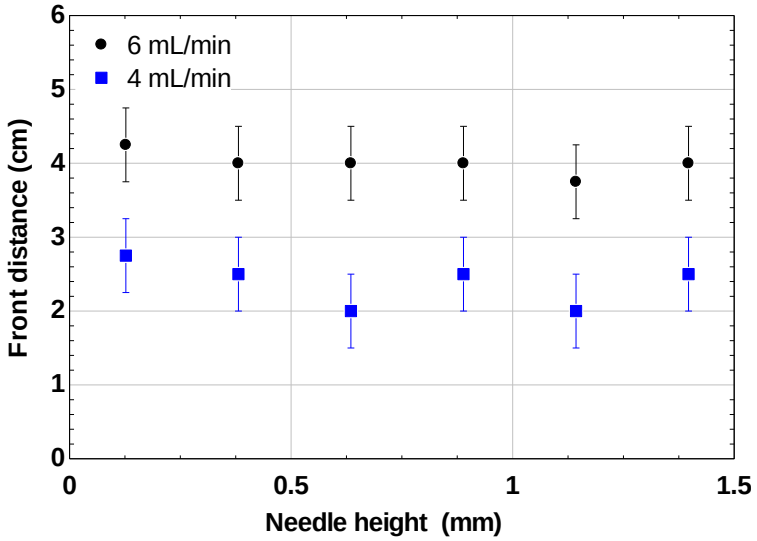

Figure 26: Front distance as a function of needle height for two different flow rates

Flow rates ranging from 2 mL/min to 8 mL/min were used in 1 mL/min increments. Above 8 mL/min, the flow consistently reaches the end of the channel. Channel gaps between 1.5 mm and 3 mm were tested in 0.5 mm increments. Figure 28 depicts the plates and post from above. Above a channel gap of 3 mm the post holding the needle no longer occupies the entire channel gap and a significant backflow of ink out of the channel is observed due to the gap between the post and plates; as a result, it is not possible to accurately measure the flow rate that passes through the channel. Below a channel gap of 1.5 mm, there is interference between the needle and the channel. Each combination of channel gap and flow rate was tested three times and the results of these three tests are averaged.

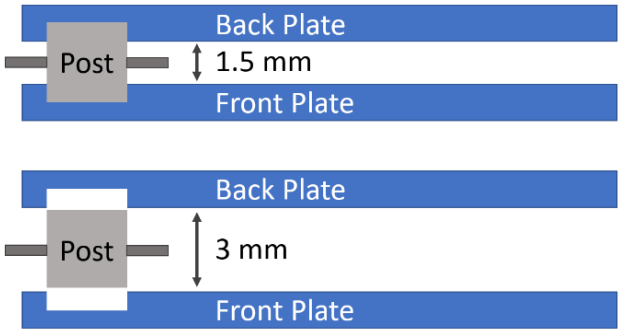

Figure 27: Schematic of experimental setup demonstrating the lower and upper limits of channel widths

The parameters that are held constant in this experiment include the static contact angle of the plates with respect to water, needle insertion height, needle diameter and needle angle; the values of these parameters are summarized in Table 1. The static contact angle is measured by placing a small drop of de-ionized water on a horizontal plate surface. The resulting contact angle is measured at five locations on the plate surface and these values are averaged. Images are taken and measurements of the contact angle are carried out using MATLAB. Prior to testing, the glass plates are rinsed with isopropyl alcohol to remove any large contaminants, then UV Ozone treated to remove any organic contaminants and to make the surface hydrophilic. This treatment yields a consistent static contact angle for water that is near 10°. Measurements of the contact angle before and after the trials show that the contact angle is unaffected by repeated trials with ink and clean water.

Table 1: Constant parameters

Parameter	Value

Solvent / Plate Contact Angle	10°
Needle height	0.75 mm
Needle angle relative to horizontal	5°
Needle inner diameter	1 mm

All data are collected in a single session according to the data collection procedure described in the previous section. Three data points for each channel width and flow rate combination were recorded and averaged. The raw data are presented in Table 2 and the averaged values are presented in Table 3. Datapoints labeled “n/a” represent conditions where the flow reaches the end of the channel, and no pooling occurs.

Table 2: Front distance data for chloroform (cm)

			Channel Gap (mm)			
			1.5	**2**	**2.5**	**3**
Flow Rate (mL/min)	**2**	**1**	0.0	0.5	0.75	1.5
		2	0.25	0.25	0.5	2.0
		3	0.0	0.5	0.75	2.0
	3	**1**	0.5	1.0	1.25	3.0

		2	1.0	1.0	1.5	1.5
		3	0.75	1.25	1.25	3.0
	4	**1**	2.5	3.0	3.5	3.75
		2	2.25	2.75	3.5	4.0
		3	2.75	3.0	3.25	4.0
	5	**1**	3.0	3.75	4.75	5.5
		2	3.5	4.0	4.25	5.25
		3	3.0	3.75	4.5	5
	6	**1**	4.5	5.75	6.5	7.5
		2	3.75	5.5	6.5	6.5
		3	4.25	6.0	6.0	7.0
	7	**1**	5.0	7.25	n/a	n/a
		2	4.75	6.75	n/a	n/a
		3	4.75	7.5	n/a	n/a
	8	**1**	7.0	n/a	n/a	n/a
		2	7.5	n/a	n/a	n/a
		3	6.75	n/a	n/a	n/a

Table 3: Averaged front distance (cm)

		Channel gap (mm)			
		1.5	**2**	**2.5**	**3**
Flow Rate (mL/min)	**2**	0.08	0.42	0.67	1.83
	3	0.75	1.08	1.33	2.50
	4	2.50	2.92	3.42	3.92
	5	3.17	3.83	4.50	5.25
	6	4.17	5.75	6.33	7.00
	7	4.83	7.17	n/a	n/a
	8	7.08	n/a	n/a	n/a

It is apparent that there is some variation in the front distance measured for a given set of conditions. One possible explanation is inherent inconsistencies in the contact angle (±3°) that are observed in solid-liquid systems [27]. The uncertainty associated with the measured data is estimated as twice the standard deviation, which is calculated by taking the square root of the variance of each group of three data points. The average standard deviation for all datapoints is found to be 0.26 cm so the uncertainty is taken to be 0.52 cm.

Figure 29 shows the measured front distance as a function of flow rate for several channel widths. The relationship between front distance and flow rate appears to be approximately linear for a given channel width. Intuitively, increasing flow rate should lead to a

larger front distance as more momentum is associated with the liquid leaving the needle which allows it to resist slowing down and eventually pooling.

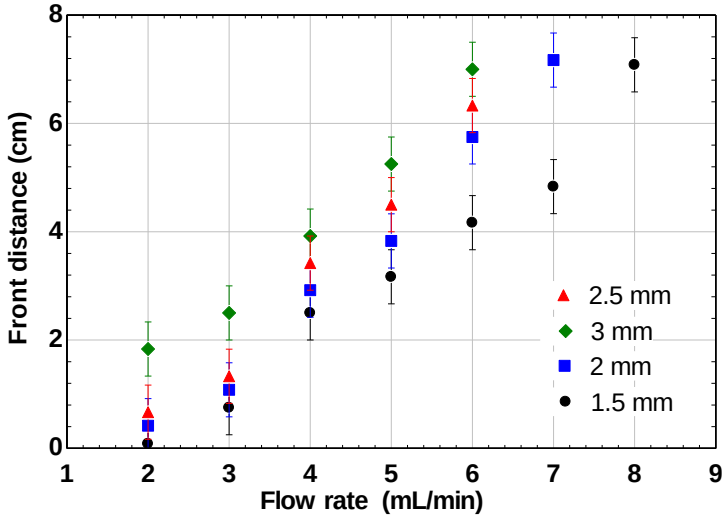

Figure 28: Front distance as a function of flow rate for various values of the channel width

Figure 30 shows the front distance as a function of channel width for various flow rates. Flow rates of 7 and 8 mL/min were excluded, as there were fewer data points for these high flow rates since the flow successfully reached the end of the channel in many of these trials. The effect of channel width is less dramatic than flow rate, but in general a larger channel corresponds to a longer front distance.

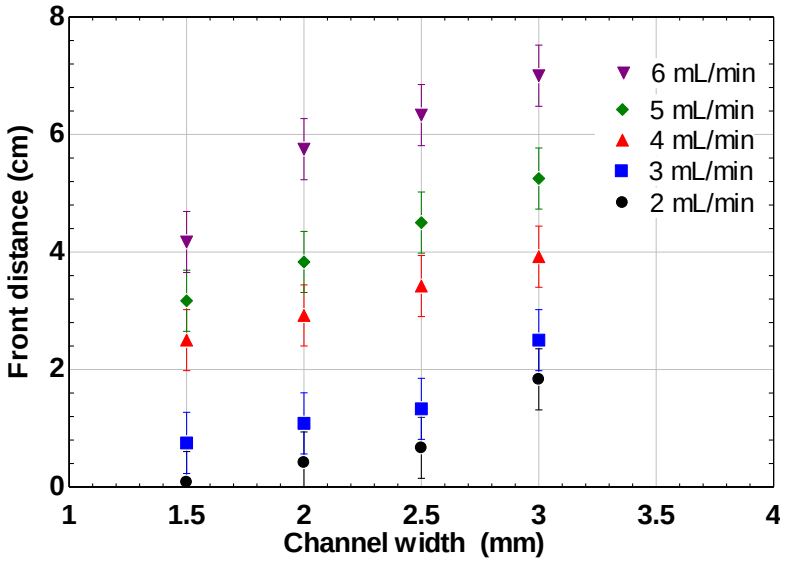

Figure 29: Front distance as a function of channel width for chloroform

Evidently, increasing either flow rate or channel width has a positive effect on front distance. To understand this relationship, the forces that govern the flow in the channel are identified and used to create a simple scaling model describing the achievable front distance in the subsequent section. This model is used together with the data to develop a semi-empirical relationship for the front distance.

3.4.5 Results and Discussion

A working model of suspended fluid flow in a thin channel can be used to understand and optimize the TaFISA process as well as other, similar solution-based materials processing methods. Such a physics-based model will help to design and scale the process without expensive trial and error. The dominant force acting to support the suspended fluid layer is the surface tension force at the ink-glass interface. The force acting to induce pooling is gravity. The

dimensionless number that compares the ratio of the gravity to the surface tension forces is the Bond number, which is generally defined according to:

$$Bo = \frac{\rho\, g\, L^2}{\sigma} \tag{1}$$

The Bond number is often used to understand the behavior of a droplet or a bubble. However, the Bond number is also relevant for liquid-liquid systems or for systems considering only a single fluid [28]. In models of dispersed multiphase fluid flows, the length scale is often taken to be the dimension of the bubbles, droplets, or particles that are suspended in the flow [29]. However, the situation studied here contains none of these discrete elements and instead the square of the length scale is replaced by the product of the radius of curvature of the meniscus at the wall, approximated as the channel width divided by the cosine of the solvent-barrier contact angle, and the ink layer height, which is proportional to the volume of the liquid that is being supported. The density is replaced by the density difference between the dense ink and less dense water, D*r*, which is the parameter that gives rise to the gravitational force. A modified Bond number is defined for this case according to:

$$Bo = \frac{\Delta\rho\, g\, w\, h}{2\,\sigma\cos(\theta)} \tag{2}$$

where σ and θ are the surface tension and contact angle, respectively, of the supported fluid with the barrier. The surface tension term is multiplied by 2 because the force is exerted on either side of the meniscus by both plates.

The modified Bond number provides a criterion for pooling; a critical Bond number of unity is assumed because in this condition the competing forces are closely balanced [28]. Situations dominated by surface tension have $Bo < 1$ while those dominated by gravity have *Bo*

> 1. Equation (3) can be rearranged and simplified to solve for the maximum film thickness that a given interface can support, or the critical thickness where the fluid layer becomes unstable:

$$h_{crit} = \frac{2\,\sigma \cos(\theta)}{\Delta \rho\, w\, g} \tag{3}$$

It should be noted that this definition is physically meaningful for channel geometries and films that result in a continuously curved meniscus (i.e., one in which the radius of curvature is directly related to the gap width). The capillary length is a fluid property that predicts the behavior of menisci by relating gravity and surface tension forces [30, 31]. The assumption that the meniscus is curved is reasonable at small channel widths, where the radius of the resulting meniscus ($w/2$) is smaller than the capillary length, given by:

$$L_c = \sqrt{\frac{\sigma}{\Delta \rho g}} \tag{4}$$

where $\Delta\rho$ is the difference in density between the solvent and air. The capillary length for chloroform is 1.35 mm, indicating the model becomes less valid at channel widths greater than 2.7 mm. At larger channel width, the solvent tends to spread to form a flat layer that behaves differently from a continuously curved meniscus. To account for this change in interface shape that occurs for large widths, the parameter w in Eq. (3) is replaced with the minimum of twice the capillary length and the channel width. Thus, at large channel widths, where the interface shape no longer changes drastically with gap width, the radius of curvature is determined by twice the capillary length divided by the cosine of the contact angle. Equation (3) is modified accordingly:

$$h_{crit} = \frac{2\,\sigma\cos(\theta)}{\Delta\,\rho\,g\,min\left(w, 2L_c\right)} \tag{5}$$

The supported ink layer is flowing on top of a water sub-phase. The actual film thickness is governed by the flow rate of the injected fluid and its velocity according to continuity. The fluids that are used as the solvents are incompressible and therefore continuity dictates that the volumetric flow rate at any point in the channel is constant. Thus, the supported fluid layer thickness h_{film} is given by:

$$h_{film} = \frac{Q}{w\,v} \tag{6}$$

where w is the gap width and v is the average (or bulk) local velocity. Figure 31 shows an exaggerated image that will result from the slowing liquid front (due to friction) causing a growing ink layer in the channel; eventually, the critical film height is reached, and the supported fluid begins to pool. The distance between this pooling location and the injection point is referred to as the front distance, L, and should be maximized to allow larger deposition areas.

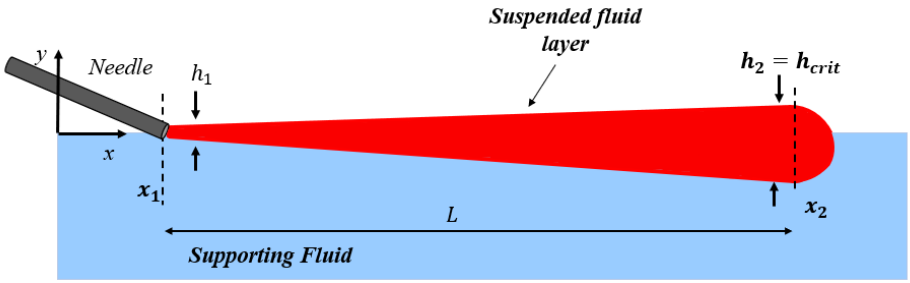

Figure 30: The supported fluid layer slows as friction acts to decelerate the front which causes its height to grow; eventually the critical height is reached which causes pooling to occur

The location where the ink is injected is x_1 and the film thickness at this location (h_1) is equal to the diameter of the needle at the start of the channel. The location downstream where the ink will pool is x_2 and the film thickness at this location is the critical film thickness. The front distance, L, is the difference between these locations:

$$L = x_2 - x_1 \tag{7}$$

The conservation of energy equation is applied between points x_1 and x_2 along a streamline in the channel separated by distance L, assuming that the flow is steady, and the fluid is incompressible.

$$\frac{P_1}{\rho g} + \frac{{v_1}^2}{2g} + z_1 = \frac{P_2}{\rho g} + \frac{{v_2}^2}{2g} + z_2 + H_f \tag{8}$$

As the fluid flows, viscous friction forces with the walls of the channel and the liquid-liquid interface act to decelerate the fluid. These losses are captured by the parameter H_f, the head loss due to friction. The channel is open to the atmosphere, so P_1 and P_2 can be assumed to be equal. The vertical height change is assumed to be small so the elevations z_1 and z_2 are also assumed to be equal. Therefore, the energy balance can be simplified to:

$$\frac{{v_1}^2}{2g} = \frac{{v_2}^2}{2g} + H_f \tag{9}$$

The head loss due to friction is approximated using the Darcy-Weisbach equation for pressure head loss in a pipe [32], where f_d is the Darcy-Weisbach friction factor.

$$H_f \approx f_d \frac{L}{w} \frac{{v_{avg}}^2}{2g} \tag{10}$$

The velocity used in Eq. (10) is the average bulk velocity in the channel (the average of the velocities at locations 1 and 2):

$$v_{avg} = \frac{v_1 + v_2}{2} \tag{11}$$

Equations (6) through (11) can be simplified and rearranged to solve for the front distance normalized by the channel width:

$$\frac{L}{w} \approx \frac{4}{f_d}\left[\frac{1}{h_1^2} - \frac{1}{h_{crit}^2}\right]\left[\frac{1}{h_1} + \frac{1}{h_{crit}}\right]^{-1} \tag{12}$$

For laminar fully developed flow, the friction factor will be inversely proportional to the Reynolds number:

$$f_d = \frac{k}{Re} \tag{13}$$

where k is a constant that depends on the channel geometry. For example, for fully developed flow between parallel plates $k = 96$ when the Reynolds number is defined based on the hydraulic diameter [32]. The Reynolds number used here is defined using the channel width, w, as the characteristic length:

$$Re = \frac{Q\rho}{\mu h} = \frac{\rho v_{avg} w}{\mu} \tag{14}$$

where μ is the dynamic viscosity of the supported fluid and v_{avg} is the average velocity given by Eq. (11). Substituting Eqs. (13) and (14) into Eq. (12) and simplifying yields an approximate relationship for the dimensionless front distance:

$$\frac{L}{w} \approx \frac{2Q\rho_{sf}}{k\mu_{sf}}\left[\frac{1}{h_1^2} - \frac{1}{h_{crit}^2}\right]\left[\frac{1}{h_1} + \frac{1}{h_{crit}}\right]^{-1} \tag{15}$$

For simplicity, the right side of Equation (15), less the constant k, is called the pooling parameter, *P:*

$$P = \frac{2\,Q\,\rho_{sf}}{\mu_{sf}}\left[\frac{1}{h_1{}^2} - \frac{1}{h_{crit}{}^2}\right]\left[\frac{1}{h_1} + \frac{1}{h_{crit}}\right]^{-1} \tag{16}$$

The approximate relationship for the dimensionless front distance is then:

$$\frac{L}{w} = \frac{P}{k} \tag{17}$$

Next, the relationship between dimensionless front distance and pooling parameter is examined using the experimental data and a correlation is developed for front distance.

A variety of organic solvents can be used to disperse nanoparticles in solution to facilitate transfer of particles to a substrate. Therefore, front distance data were also collected for chlorobenzene using the same method described above. The same range of flow rates were tested with channel widths of 1.5 and 2 mm. The properties of chloroform and chlorobenzene are given in Table 4.

It is worth noting here that it is assumed that the properties of the bulk fluid are not significantly affected by the addition of nanoparticles, in this case single wall carbon nanotubes (SWCNTs). A typical concentration of SWCNTs for TaFISA is 100 µg/mL, which corresponds to a percentage by weight in chloroform of 6.7%. Literature suggests that surface tension of solutions containing multiwall CNTs (MWCNTs), which are larger in diameter and length, only slightly affects the bulk fluid surface tension. In the case of Ref. [33], a 5 wt. % addition of MWCNTs corresponds to a 1% decrease in surface tension of the bulk ethylene glycol solution. Regarding other fluid properties such as dynamic viscosity, the addition of nanoparticles may have a significant effect. The work by Xiaoke demonstrates that with 5 wt. % addition of MWCNTs, the viscosity of the base fluid (water) increases by 22 times. This effect is likely sensitive to other factors such as the base fluid, the nanoparticle size, and the presence of a

stabilizing agent to maintain individualization of the nanoparticles [34]. In the author's experience, experimentation with the addition of 100 μg/mL of SWCNTs has not demonstrated a significant deviation from the results shown here. It is likely that in other systems with different base fluids and nanoparticle types and concentrations, the nano-particle concentration will have a significant effect on the fluid properties. The dimensionless front distance measured for both chloroform and chlorobenzene are plotted as a function of the pooling parameter, *P*, in Fig. [X].

Table 4: Fluid properties and friction factors of the test fluids

	Chloroform	**Chlorobenzene**	**Water**
Density (ρ)	1.5 kg-m^{-3}	1.1 kg-m^{-3}	1.0 kg-m^{-3}
Dynamic viscosity (μ)	0.55 mPa-s	0.80 mPa-s	1.0 mPa-s
Static Contact Angle (θ)	10°	10°	10°

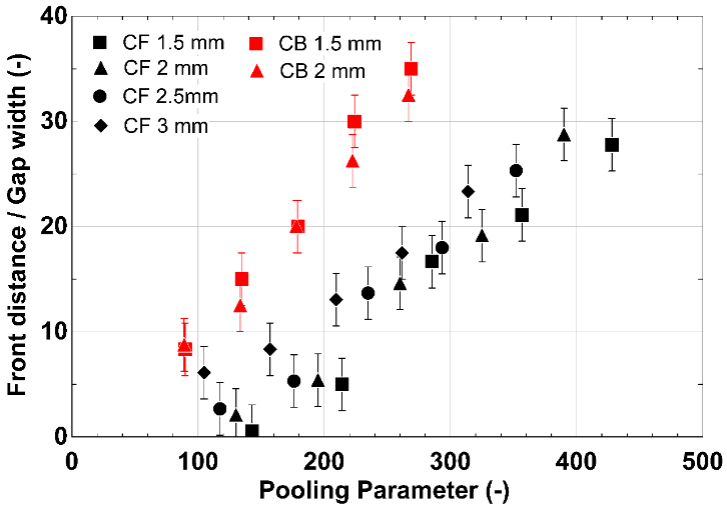

Figure 31: Dimensionless front distance as a function of Pooling parameter for chloroform (black) and chlorobenzene (red)

Notice that the data for each fluid collapse separately with an approximately linear relationship. Ideally, the data for both fluids should collapse to a single line since the model considers fluid properties. This suggests that the friction factor coefficient, *k*, may not be

identical for both fluids. Therefore, it is worth evaluating the assumptions made about the friction factor *k* in Eq. (13) to confirm that they are appropriate. The use of a single *k* value assumes that the flow in each case is laminar and fully developed. Even for high flow rates, the Reynolds number for both fluids remain in the laminar regime. To evaluate the assumption that flow is fully developed, the hydrodynamic entry length for internal flow [35] is computed according to:

$$x_{fd} \approx 0.06\, Re\, D_h \tag{18}$$

where D_h is the hydraulic diameter.

By inspection of Eq. (18) and the fluid properties, chlorobenzene becomes fully developed more quickly than chloroform, by approximately a factor of two. Therefore, it is reasonable that the friction factor parameter *k* will be smaller for chlorobenzene than it is for chloroform, where the hydrodynamic entry length is a significant fraction of the channel length. The geometry associated with the flow in this experiment does not conform to a typical, confined internal flow and therefore it is not possible to precisely predict the *k* values based on literature. Here, the friction factor *k* absorbs the effects of unknown factors such as the impact developing length in this unique channel geometry.

Using the data in Figure 32, it is found that the most appropriate value of *k* for chlorobenzene is $k_{cb} = 10$ whereas the friction coefficient for chloroform is $k_{cf} = 20$. Note these differ by a factor of 2; this difference may be related to the difference in fully developed length explained by Eq. (18). Using these parameters, the measured dimensionless front distance as a function of the ratio of the pooling parameter to the friction factor parameter *k*, Eq. (17), is shown in figure 33. Also shown in figure 33 is the best fit and ±15% deviation lines.

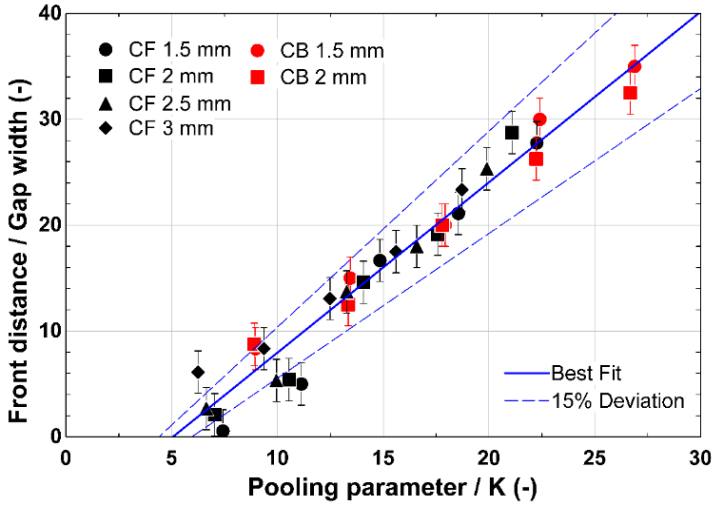

Figure 32: Front distance normalized by gap width as a function of the pooling parameter for chloroform and chlorobenzene

Using these values of the friction coefficient, the data for both fluids collapsing to a single line. Over 80% of the data fall within ±15% of the best fit line, suggesting a strong relationship between dimensionless front distance and the pooling parameter divided by the friction coefficient. It is worth noting that at low flow rates the effects of friction and surface tension are relatively high, and these are less controllable, leading to a lower degree of certainty, as seen in figure 33. The best fit line yields a correlation for front distance as a function of gap width, pooling parameter, and the friction coefficient:

$$L = w\left[1.61\left(\frac{P}{k}\right) - 8.14\right] \tag{19}$$

$$P = \frac{2\,Q\,\rho_{sf}}{\mu_{sf}}\left[\frac{1}{h_1^{\,2}} - \frac{1}{h_{crit}^{\,2}}\right]\left[\frac{1}{h_1} + \frac{1}{h_{crit}}\right]^{-1} \tag{16}$$

$$k_{cb} = 10,\ k_{cf} = 20$$

Equation (19) describes the relationship governing the front distance for a supported fluid layer flowing between parallel plates, and is dependent on the channel geometry *w*, a dimensionless pooling parameter *P*, and the friction coefficient parameter *k*, which equals 10 and 20 for chlorobenzene and chloroform respectively. Recall the pooling parameter, defined in Eq. (16) is a function of fluid properties, the initial fluid layer thickness, h_1 (or more simply the inlet diameter), and the critical fluid layer thickness, h_{crit} which is determined using the modified Bond number. The correlation simplifies the complex relationship between the buoyancy, surface tension, gravity, and friction forces as they affect the front of a flowing suspended fluid. It also helps to identify the impact of parameters such as channel width and flow rate on pooling behavior. Understanding these relationships is an important step in scaling solution-based materials processing methods that rely on liquid-liquid interfaces, such as TaFISA. The next section applies the correlation to make predictions about front distance and to suggest methods for avoiding pooling.

3.4.6 Methods to improve front distance

The objective of the experimental and modeling work in this study is to understand the behavior of a dynamic front confined in a thin channel and to identify methods that can be used to increase front distance. Figure 34 shows the front distance as a function of gap width for various values of flow rate predicted by the correlation given in Eq. (19), overlayed with experimental data.

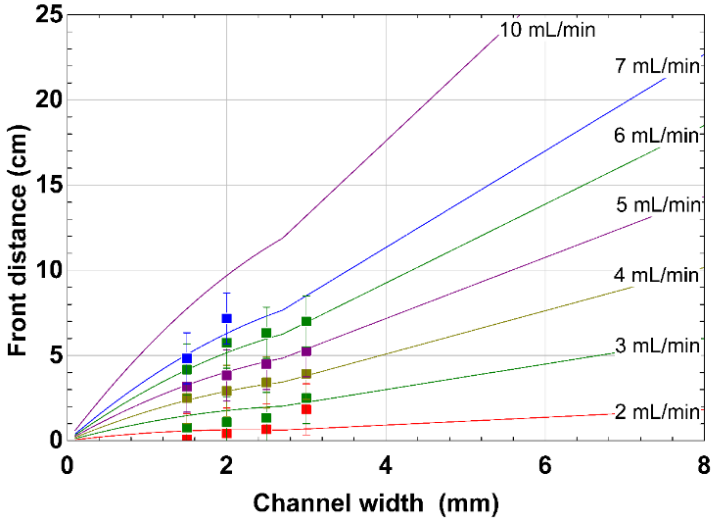

Figure 33: Correlation results from Eq. (17) and data for chloroform front distance as a function of the channel width for various values of flow rate

The correlation predicts an inverse parabolic relationship between front distance and channel width until the channel width becomes larger than $2L_c$, at which point front distance begins increasing linearly. This relationship can be explained conceptually by the balance between friction and surface tension forces. Small channel widths lead to much higher losses due to friction that act to quickly decelerate the front and encourage a growing fluid layer. As channel width increases, losses due to friction are less significant and the front can move more easily through the channel. As channel width increases further, the surface tension forces remain relatively constant, and the fluid behaves as it would on a featureless water surface.

The practical application of the model lies in its ability to predict the general trends that are observed as flow rate, channel width, and fluid properties are varied. For example, if a given deposition method requires suspended flow across a 10 cm substrate, figure 34 can be used to select a flow rate and channel width combination favorable to the deposition parameters. This example case would suggest a flow rate near 7 mL/min and a channel width near 4 mm.

Solution based deposition methods like TaFISA often depend heavily on the fluid conditions during the deposition process. This usually means operating within the laminar flow regime in order to avoid turbulent eddies near the interface, which can lead to poor deposition quality [16]. It follows that in many cases higher flow rates are undesirable, despite being one of the simplest methods to increase front distance. For example, an 18 cm substrate might suggest flow at 10 mL/min in a 5 mm channel width to reach the desired front distance. These conditions result in a Reynolds number nearing the transition to turbulence which would be undesirable, and lead the user to select a lower flow rate, 7mL/min, and larger channel width, such as 7 mm.

For conditions where laminar flow is critical, the model helps identify other methods of increasing front distance. For example, the critical film thickness given by Eq. (5):

$$h_{crit} = \frac{2\,\sigma \cos(\theta)}{\Delta\rho\, g\, min\left(w, 2L_c\right)} \tag{5}$$

suggests that increasing the contact angle can increase the critical thickness drastically, which might point to a surface treatment in order to improve front distance. If possible, it also suggests using a lower density solvent, a higher density liquid subphase, or a solvent with a small capillary length.

Another promising method of increasing front distance is to add an additional stabilizing term to the energy balance given in Eq. (9):

$$\frac{{v_1}^2}{2g} = \frac{{v_2}^2}{2g} + H_f \tag{9}$$

In this equation, the water surface is assumed to be flat so that the vertical height change may be taken as being insignificant. However, an additional favorable potential energy term could be used to increase front distance. Using the laws of capillary rise between parallel plates

[36], a downhill slope can be induced by using a tapered channel that expands in the flow direction. Near the channel entrance the meniscus is pulled up to higher elevation, which introduces a height differential Δh into the energy balance:

$$\frac{v_1^2}{2g} + \Delta h = \frac{v_2^2}{2g} + H_f \tag{20}$$

This height change can be expressed in terms of the density, ρ_w, contact angle, $\theta_{w,air,}$ and surface tension, $\sigma_{w,air}$ of the supporting fluid (water) with respect to air. The law of capillary rise between parallel plates is applied [36]:

$$\Delta h = \frac{2\sigma_{w,air}\cos(\theta_{w,air})}{(\rho_w - \rho_{air})\, g\, w_1} - \frac{2\sigma_{w,air}\cos(\theta_{w,air})}{(\rho_w - \rho_{air})\, g\, w_2} = \frac{2\sigma_{w,air}\cos(\theta_{w,air})}{(\rho_w - \rho_{air})\, g}\left(\frac{1}{w_1} - \frac{1}{w_2}\right) \tag{21}$$

Even a small taper added to the channel results in a relatively significant potential energy term. Table 5 shows several combinations of channel widths, where w_1 is the width at the injection point and w_2 is the width near the exit of the channel, and the associated height change Δh. For context, the initial velocity head (i.e., the kinetic energy term) in Eq. (20) for a flow rate of 8 mL/min is only 0.43 mm.

Table 5: Spacer Values and Δh

w_1(mm)	w_2(mm)	Δh(mm)
1.5	1.5	0
1.5	2	2.0
1.5	2.5	3.3
1.5	3	4.1
1.5	3.5	4.6

The effect of tapering the channel width was examined experimentally through tests with chloroform. Measurements were made using a channel width near the needle of 1.5 mm that increased to 2.5 mm at the exit, corresponding to a Δh of approximately 3.3 mm. Front distance is measured and overlayed onto the constant channel width results that were shown in figure 33; these additional results are shown in figure 35. The dimensionless front distance and pooling parameter for the taper are each calculated using the average channel width of 2 mm for these data. For a given flow rate and average channel gap, the tapered channel provides a significant improvement on front distance, allowing the use of lower flow rates and channel gaps for a given channel length.

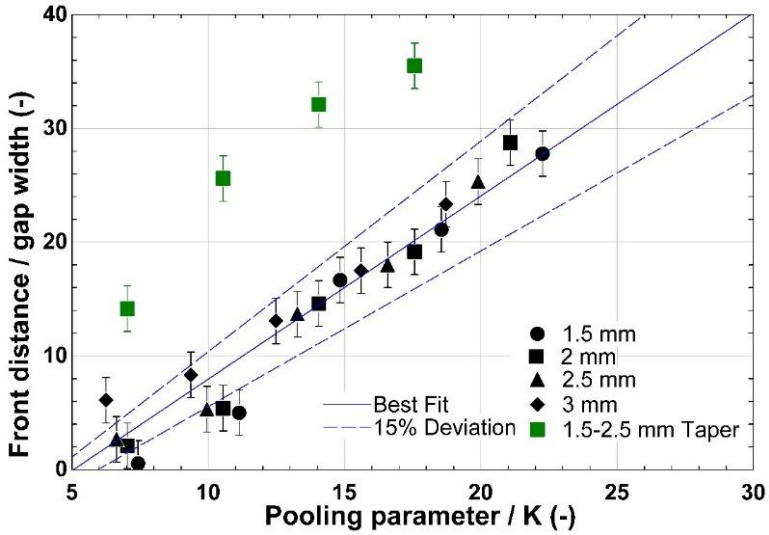

Figure 34: Front distance normalized by gap width as a function of the pooling parameter over friction factor for chloroform with a straight and tapered channel

The model presented here allows for front distance to be scaled to larger values, which opens the possibility for methods such as TaFISA to be scaled up to larger wafers. An understanding of the physics governing stratified flow within the channel formed between parallel plates helps to define the practical working conditions of solution-based materials processing methods as well as to understand various methods for increasing front distance, such as altering fluid parameters, channel width, and channel geometry.

3.4.7 Conclusion

Solution-based deposition methods represent a promising route to depositing wafer-scale arrays of aligned CNTs for high speed and low power semi-conductor electronics. Especially promising are solution-based methods that exploit the formation of a 2D nematic liquid crystal at the liquid-liquid interface between water and nanoparticles dispersed in an organic solvent to achieve high packing density and alignment. These methods also present unique challenges that become significant as the process scales, such as the pooling and sinking behavior described here.

The work presented here develops a simple, semi-empirical model that identifies the significant forces governing suspended stratified flow between parallel plates and offers a correlation to predict front distance given a system geometry and fluid parameters. This model is shown to be accurate for multiple fluids to within about $\pm 15\%$ of the experimental data. This correlation can be used to select experimental parameters such as flow rate, channel width, and channel geometry to achieve a desired channel length when scaling solution-based deposition methods. It also suggests an optimal solution space to aid in the design of solution-based materials processing methods where fluids of differing densities are used in contact with one

another. Finally, the model was used to identify a method that substantially increases front distance through the introduction of a minor taper to the channel.

The model can be improved to account for changes in channel geometry (e.g., a sudden step change in the channel), changes in channel angle (arranged at 45° with respect to gravity as opposed to vertically) or changes in injection angle. The model could also be improved with further testing using more organic solvents with an apparatus that can test at higher flow rates and channel widths. As solution-based deposition methods for depositing aligned arrays of CNTs and other nanoparticles grow in scale, a deeper understanding of the forces governing the stability of a supported fluid layer will become even more important in the design of reliable, efficient, and practical methods.

4 Oscillating Shear Induced Alignment (OSA)

4.1 Introduction

As modern field effect transistors become smaller, they approach a minimum size beyond which their performance is significantly reduced, effectively enforcing a limit on the size and overall efficiency of these critical devices [37]. Semiconducting single-walled carbon nanotubes (SWCNTs) provide a promising alternative for next-generation field effect transistors (FETs). SWCNTs boast exceptional charge transport properties at small channel widths beyond those currently achievable by the MOSFET [5-8] and can be processed in solution; CNTs are incorporated into an organic solvent solution to form a CNT "ink" which can be easily manipulated and deposited onto a target substrate to form a uniform thin film of CNTs.

In order to exploit the full potential of SWCNTs for thin film electronics, they must be deposited in uniformly aligned and densely packed arrays which act as the foundation upon which FET devices are constructed. A poorly aligned film has many crossing CNTs that introduce nanotube-nanotube junctions which act to increase resistance. A low packing density means fewer charge conducting pathways which causes poor on-current and mobility. Thus, controlling alignment and density is the primary challenge facing the adoption of CNTFETs in industry [38].

The cost, time, and effort necessary to produce uniformly aligned and densely packed arrays of CNTs with consistent quality is a major barrier to producing CNTFETs on a larger scale. Many methods exist to deposit randomly oriented films of CNTs, such as drop-casting [39], spray coating [40], and vacuum filtration [41], but these films are unsuitable to make to make a high number of quality devices. Several solution-based methods have been demonstrated

to deposit aligned arrays of CNTs, such as shear alignment [9], evaporative self-assembly [10], directed evaporation, [11,12], Langmuir Blodgett and Schaeffer methods [15], among others. While these methods are promising, none have been proven to solve the issues of cost, scalability, and control over alignment and density that is required for manufacturing high-performance devices on a large scale.

Viscous shear as a method for aligning elongated nanoparticles has been explored extensively in recent years as it relates to many fields such as biology [42] additive manufacturing [43], and nanocomposite materials [44]. Velocity gradients within a fluid under shear produce a shear force which acts to align elongated particles with the flow direction. This effect is dependent on factors such as the shear rate and the rotational diffusion coefficient, a measure of how freely a particle can rotate in solution. In Ref. [42] pressure-driven oscillatory shear flows in microfluidic channels are shown to elongate and align DNA molecules, allowing for better imaging conditions. Shear rate and thus alignment is determined to be a function of flow rate and channel geometry. Understanding the relationships between shear rate and alignment and determining the optimal solution space for aligning SWCNTs under shear driven flows is a major focus of this paper.

Here a novel method is proposed for depositing aligned arrays of SWCNTs using sinusoidal oscillatory shear, called oscillating shear alignment (OSA). OSA achieves deposition across the majority area of the target substrate with uniformity and a high degree of alignment. While several methods have been proven to deposit aligned arrays of nanoparticles in microfluidic channels over small areas [45], few have utilized shear to deposit films over a large area with high uniformity. One such method, substrate-wide confined shear alignment, utilizes a thin, (sub-mm) channel to produce large areas of aligned CNTs across an entire substrate via

fluid shear [9], and relationships for alignment degree and packing density are determined. The work here aims to explore the relationships governing alignment and density using a drastically different experimental apparatus which produces a sinusoidal oscillatory shear pattern within a small cavity. This not only strengthens the understanding between factors such as shear rate, alignment, concentration, and packing density, but provides an alternative scalable deposition method for producing aligned arrays of SWCNTs.

4.2 Fluid shear modeling

In order to accurately develop relationships between the degree of alignment and shear rate for a sinusoidal oscillatory shear pattern, a reasonable estimation of the shear rate must be known for a given amplitude and frequency. This section describes the formulation of the numerical model used to calculate the shear rate given a set of input parameters.

The experimental setup used here allows a user to select a motor speed (frequency) to rotate a specially designed cam, which translates simple harmonic rotational motion to sinusoidal linear motion of the target substrate. The cam profiles are generated in MATLAB using a script provided in Ref. [46]. Each cam has a specified "lift" which corresponds to the sinusoid's amplitude. Using this amplitude and frequency, the sinusoidal forcing function for the substrate position is of the form:

$$s(t) = (A)\sin(\omega\, t) \tag{22}$$

Where *s(t)* is the velocity at a given distance from the substrate, *y*, and time, *t*. *A* is the amplitude of oscillations in meters (also referred to as the cam's "lift"), and ω is the frequency in radians/second. Using stokes solution for oscillatory Couette flow, shear rate is calculated as a function of *y*, distance from the substrate, given a forcing function describing the substrate's

motion [47,48]. The fluid velocity as a function of distance from the oscillating substrate, *y*, and time, *t* is:

$$U(y,t) = \frac{U_{max}}{2\,[\cosh(2\lambda L) - \cos(2\lambda L)]}\left[e^{-\lambda(y-2L)}\cos(\omega t - \lambda y) + e^{\lambda(y-2L)}\cos(\omega t - \lambda y) - e^{-\lambda y}\cos(\omega t - \lambda y + 2\lambda L) - e^{-\lambda y}\cos(\omega t + \lambda y - 2\lambda L)\right] \quad (23)$$

Where L is the substrate-wall distance, and λ is given by:

$$\lambda = \sqrt{\frac{\omega}{2v}} \quad (24)$$

The solution assumes that the substrate and cavity are infinitely long so that velocity is not a function of position on the substrate, *x*, but only as a function of *y*, or distance from the substrate. This solution also assumes that the depth of the substrate, fluid, and stationary wall extend infinitely into the page, and the three cavity walls (excluding the stationary wall nearest the substrate) are far away, and their influence is negligible. A simplified schematic of the fluid cavity and substrate as seen from above is shown in figure 36.

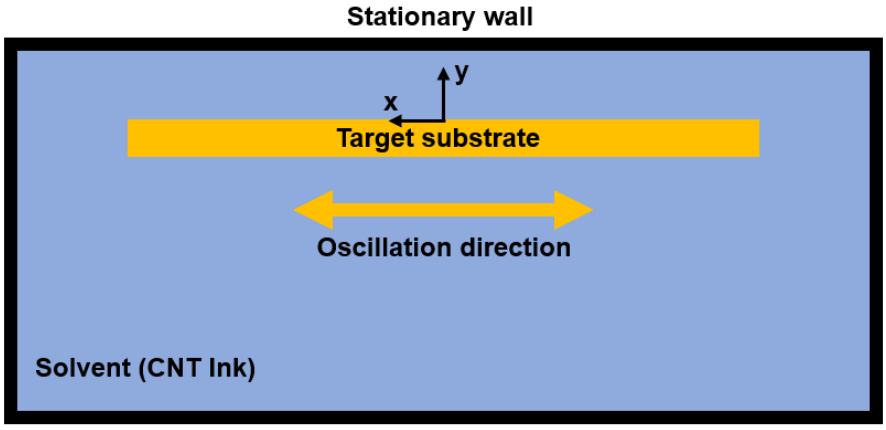

Figure 35: Schematic of oscillating substrate within a stationary cavity filled with solvent

Using Equations (23) and (24) to calculate the fluid velocity field, the shear rate at the substrate can be calculated by dividing the velocity gradient by a sufficiently small Δy, in this case taken to be 0.025 mm, or 1/50th of the substrate-wall distance, L. The shear rate as a function of time is given by:

$$\tau(t) = \frac{U(y=0,t) - U(y=0.025,t)}{\Delta y} \tag{25}$$

With Eq. (25), the instantaneous, maximum, and RMS shear rate can be calculated for a given frequency and amplitude of substrate oscillation. It should be noted that the relevant shear value related to alignment for a continuously changing substrate velocity is not well known, as it is for the case of continuous, unidirectional shear. For this consistency, the maximum shear value experienced at the substrate wall is used here.

Using Equations (23-25), the steady state substrate velocity and shear rate are plotted as a function of time on figure 37. Notice the shear rate is out of phase with velocity, reaching its peak before the maximum velocity is reached. This is due to the existence of a flow reversal due to the changing direction of the substrate. At some point the flow that is being dragged along with the substrate in the positive direction must slow and reverse direction after the substrate begins moving in the opposite direction. It is shortly after this reversal where the fluid shear rate is at its maximum.

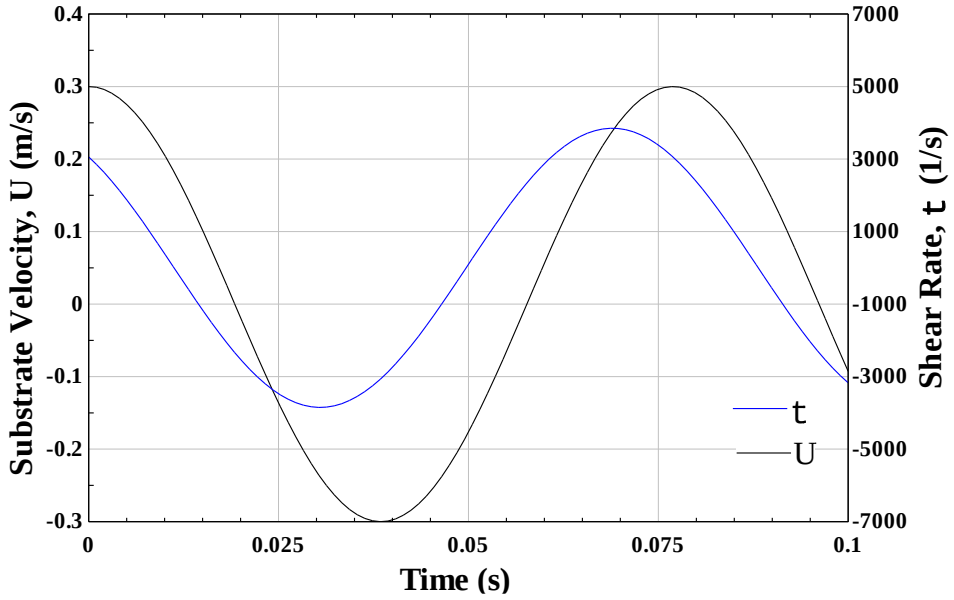

Figure 36: Steady state substrate velocity and shear rate as a function of time

Using this solution, the effects of substrate-wall distance, frequency, and amplitude can be quickly evaluated. Such a model, although not a precise solution, is very useful in design of the experimental apparatus, as knowing the required acceleration and velocity of the substrate can help to size components such as motors and linear rails. Additionally, parametric studies can be run quickly to evaluate the effect of changing multiple variables. For example, a plot of RMS shear rate as a function of substrate-wall distance for various values of amplitude and frequency is shown in figure 38.

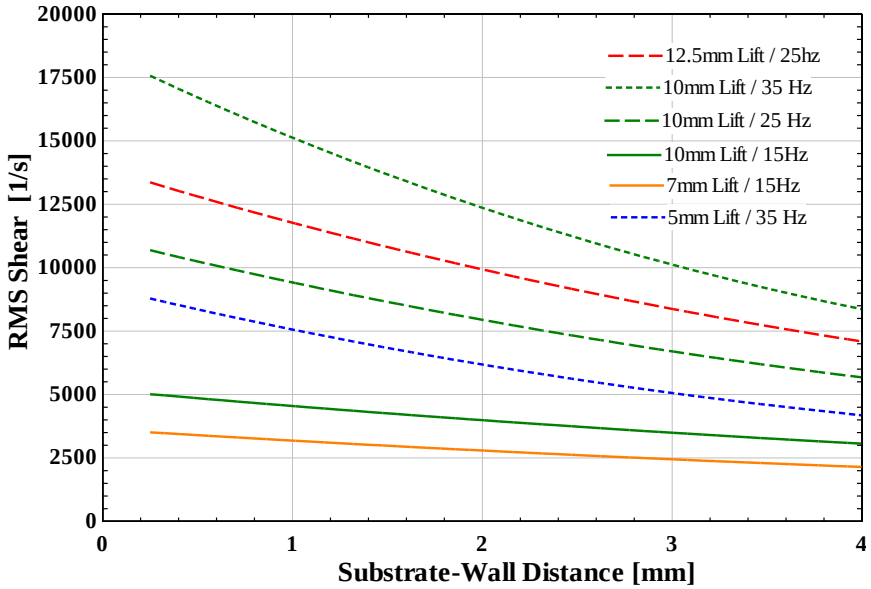

Figure 37: RMS shear as a function of substrate-wall distance for a variety of frequency and amplitude combinations

Note that increasing both amplitude and frequency acts to increase the RMS shear rate. Also, decreasing the substrate-wall distance increases the shear rate similarly. For all experiments performed here, the substrate-wall distance remained fixed at L=1.33 mm.

The analytical solution to stokes problem is used here to determine the frequency and amplitude of oscillations necessary to evaluate the effect of alignment at various shear rate conditions. The following sections describe the experimental apparatus and procedure for depositing CNT films using oscillating shear.

4.3 Experimental apparatus

Several images of the experimental apparatus is shown in figure 39. Several critical components are labeled. The top of the substrate is secured to a machined aluminum plate with a toggle clamp (A), which can be raised and lowered from the cavity during depositions. This plate

is secured to a linear carriage (B) mounted on a precision linear rail (C) so the linear motion of the substrate is constrained to a single plane. This linear rail, as well as several other components, are fixed to a rigid frame made from aluminum extrusion (D). The carriage is driven by a simple harmonic motion cam mounted on a high-speed, high-torque DC motor (E). The motor speed (and oscillation frequency) is controlled using an Arduino Nano microcontroller paired with an L298N hall effect motor controller (F). The Arduino measures the pulses directly from the hall sensors on the motor to display an accurate, instantaneous measurement of the motor frequency. On the opposite side of the linear carriage, two springs (G) provide the opposing force necessary to keep the carriage in constant contact with the cam at high speeds.

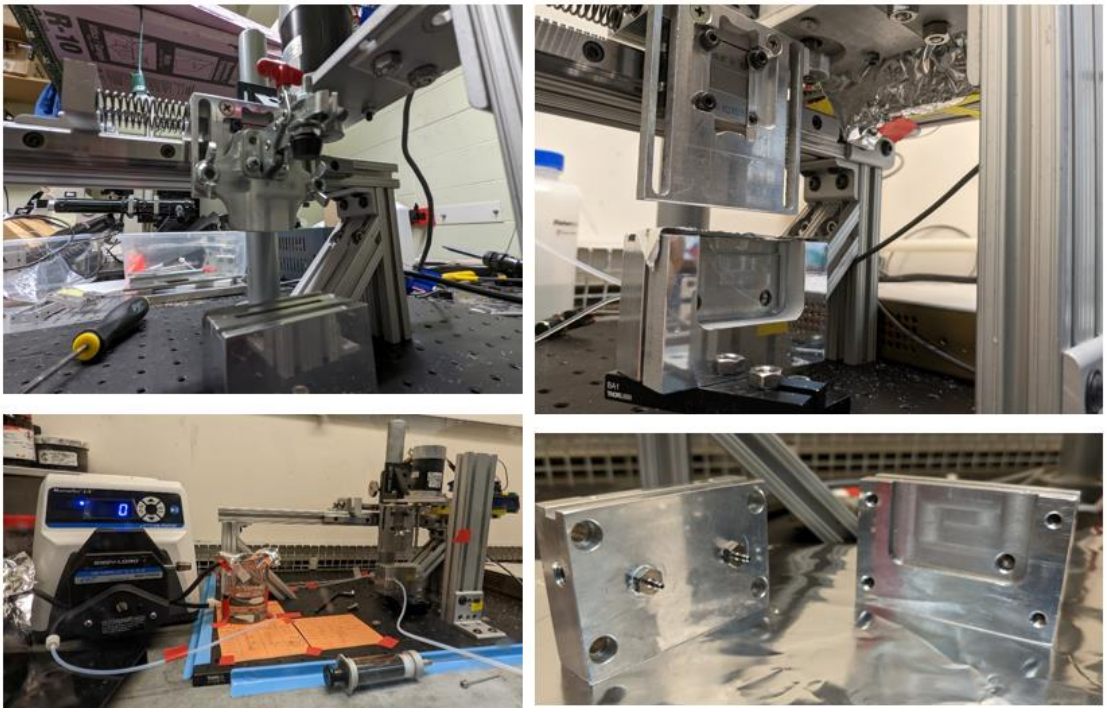

Figure 38: Experimental apparatus used to oscillate the target substrate submerged in a cavity filled with CNT ink

Below the substrate, a two-part aluminum cavity (H, I) is fixed to the table. A closer view of the cavity is shown in the bottom right of figure 39. The cavity contains the small 8 mL

volume of solvent / CNT ink used during a deposition. The cavity also contains three separate ports used for injection and removal of solvent / CNT ink, automated by a syringe pump or peristaltic pump (J), depending on the deposition type and configuration. The machined aluminum surface on which the substrate is fixed is used to align the cavity parallel to the oscillation direction to minimize any irregular effects from misalignment between the substrate and the cavity wall. To minimize fluid motion at the free surface exposed to air, a small PTFE baffle with a small slit for the substrate is inserted into the cavity.

4.4 Data collection

Several deposition styles were explored with this apparatus, all of which are slight modifications of one another. During a standard deposition, the substrate begins submerged in a clean solvent (chloroform, in this case). The motor, with the selected cam attached, is then set to the desired speed (frequency). Next, a small volume of concentrated CNT ink is injected though port A on the side of the cavity. Through experimentation with a modified cavity containing a glass window, the assumption that the concentrated ink becomes well mixed quickly is observed and verified.

Following ink injection, the substrate is allowed to oscillate in the CNT ink for a prescribed amount of time, until the peristaltic pump is activated, and clean solvent is pumped into the cavity through port B while the mixed CNT ink is removed at the same rate through port C. This reduces the concentration of the ink while the substrate is in motion. The recorded exposure time is a combination of two numbers, the time exposed to the fully concentrated ink, and the time it is exposed to the diluted mixture until the substrate motion is paused. Previous experimentation suggests that if the stationary substrate is exposed to CNT ink, CNTs will

deposit randomly without shear to align them. Once the cavity is adequately diluted to < 5% of the initial concentration, the motor is turned off and the substrate removed, rinsed with IPA, and dried using compressed air. To remove excess polymer from the surface, the sample is then boiled in toluene for 60 minutes.

The quantities of interest in this study are primarily alignment and packing density. For the films studied here, this data is collected by manually tracing images of the individual CNTs using high magnification SEM images. For this reason, a minimum of five SEM images are taken at several locations across the substrate and averaged to obtain an accurate overall measure of alignment across the entire substrate. Images are traced using *ImageJ*, which records the angle relative to the horizontal and the length of each CNT.

It should be made clear that in some cases, localized areas of uncharacteristically poor alignment are present. From the author's experience, these regions are outliers and represent a small percentage of the sample. In these cases, these regions are ignored and only the images that provide an accurate representation of the global alignment are used to collect data. Thus, it should be made clear that the data here represents the upper limit of the alignment that is achievable with OSA in its current configuration.

Each sample corresponds to a single datapoint, which is an average of several SEM images containing anywhere from 25 – 1000 CNTs each, depending on the test conditions. A minimum of 1000 total CNTs are traced and averaged for each datapoint, but in many cases, the number of CNTs per datapoint is greater than 1000. To provide a worst-case scenario for error, the maximum observed error of ± 5° is assumed for all datapoints moving forward. Although most CNTs deposit as a relatively straight line, it is possible a CNT deposits with a curved shape. In these cases, the CNT is divided into 2 segments, from each end to the middle. Although this

artificially increases the amount of short CNTs measured, the primary goal is to measure the alignment, for which this is a better measure of the large deviation of a curved tube than would be traced end-end. Ultimately, less than 10% of CNTs deposit with a curved shape, so the effect of this measurement technique is small.

ImageJ records the angle and length of each CNT in pixels. The lengths are calibrated with the scalebar on the SEM image, and the angles are modified to fall between -90 and 90 degrees, where an angle of 0º corresponds to the horizontal, or the oscillation direction. With this data, the alignment distribution, length distribution, and standard deviation can be obtained. The chosen measure of alignment is half-width at half maximum (HWHM), half of the full-width at half maximum (FWHM). For a normal (Gaussian) distribution, the FWHM corresponds to the difference between the two values of the independent variable measured when the dependent variable equals half its maximum value. Equation (26) gives the conversion from standard deviation σ to HWHM:

$$HWHM = \frac{2.355\,\sigma}{2} \tag{26}$$

There are several methods to measure packing density of a CNT film. The more straightforward method is ideal for samples with sparse films. This method simply divides the total number of traced CNTs by the total area measured. This metric gives an area density with units of CNTs/μm^2. The second method is preferred for films with moderate-high packing density and involves tracing a vertical line (perpendicular to the alignment direction), and manually counting the CNTs which intersect this line, and diving by the vertical length. This is performed at several locations across several images to obtain an average value. This method yields a line density with units of CNTs/μm. Where possible, the line density is the preferred

metric, but for sparsely populated samples the line density has a very high variation depending on the position and length of the vertical line. It is important to note that because the location of the line is chosen manually, there is bias to select the more densely packed areas. It should be clear that the linear density metric here represents an upper limit of linear packing density achievable with OSA.

4.5 Results and discussion

Experiments are conducted in order to test the effect of shear rate, concentration, amplitude, frequency, and CNT length on the quantities of interest, mainly degree of alignment and linear packing density. In this study, cams with amplitudes of 1mm, 1.5mm, 3mm, and 7.5mm are tested. Frequencies varied from 0-100 Hz, and depending on the amplitude, the resulting shear rate fell within the range 0–8600 s^{-1}. Cavity concentrations varied from 15 µg/mL to 150 µg/mL, and total exposure time was within 60 – 300s. The remainder of this section explores the relationships between these and the resulting data for alignment and density.

4.5.1 Alignment

For unidirectional, continuous fluid flow, degree of alignment of long particles increases with shear rate [9,49]. Equations (27) and (28) shows the formula for the average shear rate γ in a simple rectangular duct [50]*:*

$$\gamma = \frac{Q\,P\,\lambda}{8\,A^2} \tag{27}$$

Where Q is the volumetric flow rate, P is the wetted perimeter, A is the cross-sectional area, and λ is the shape factor, a function of the width (a) and height (b) of the rectangular duct:

$$\lambda = \left[\left(1 - 0.35\frac{b}{a}\right)\left(1 + \frac{b}{a}\right)\right]^2 \quad (28)$$

Evidently, shear rate increases with the volumetric flow rate, the wetted perimeter, and the shape factor, while shear rate decreases with cross sectional area of the channel. This implies that the highest shear rates occur with high flow rates through very small, thin channels. For a given test apparatus, the channel geometry remains constant, so shear rate is primarily a function of the volumetric flow rate. For the sinusoidal oscillating shear case used here, shear rate is a more complex function of frequency, amplitude, and substrate-wall distance (refer to Equations (23)-(25) above). For this reason, it is beneficial to evaluate degree of alignment as a function of not only shear rate, but also amplitude and frequency, to determine if either parameter has a more significant effect on degree of alignment.

Figure 40 shows HWHM as a function of maximum shear rate with a fixed amplitude of 1.5 mm, and includes several representative images at low, moderate, and high shear rate. Note that all data shown here use batches of ink with similar length distributions.

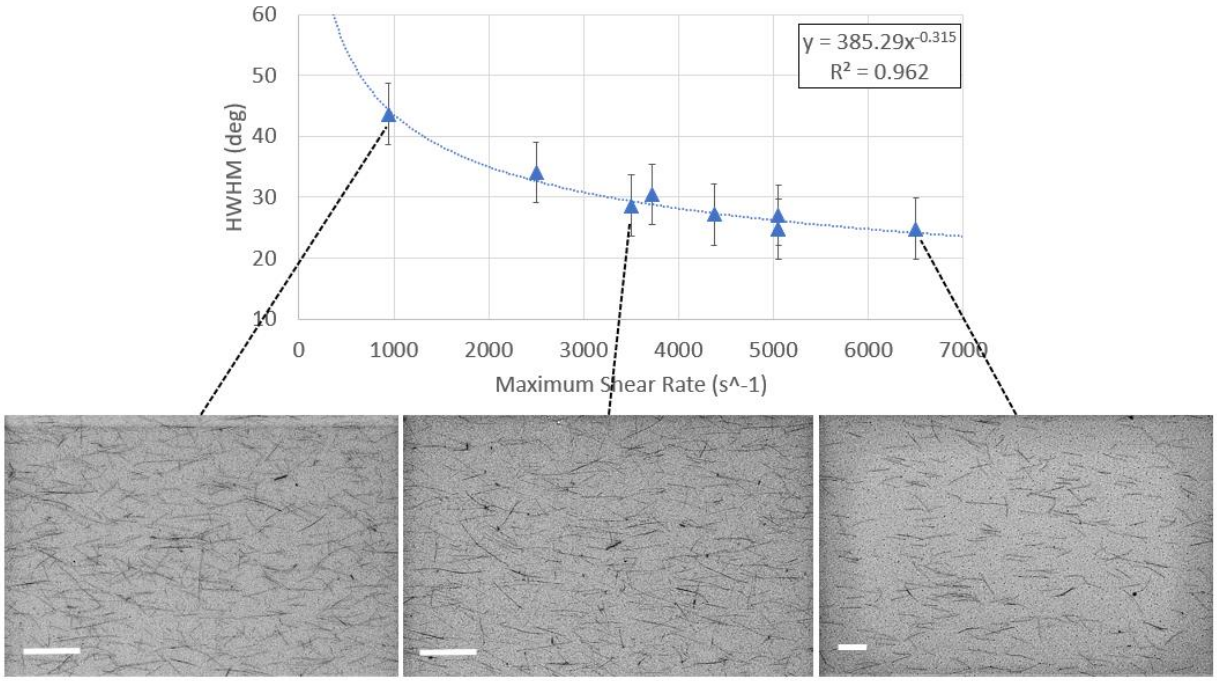

Figure 39: HWHM as a function of Maximum shear rate, with selected images at various shear values. Scalebar shown is 1 um

From figure 40, several conclusions can be drawn. The first is that alignment is a function of shear rate according to the power law relationship given by Equation (29), with an R^2 value of 0.96:

$$HWHM = 385\ (\gamma^{-0.31}) \tag{29}$$

The second conclusion is that the largest improvements in alignment occur at relatively low values of shear rate. HWHM improves by 10° for a 1500 s^{-1} increase from 1000-2500s^{-1} shear rate. A similar increase from 3500-5000s^{-1} only yields a 4° improvement in HWHM. This trend appears to continue at higher shear rates. This implies that to continue to increase shear rate at high degrees of alignment, proportionally higher values of shear rate must be achieved.

Figure 41 shows the same set of data plotted versus frequency instead of shear rate. It shows a very similar trend, with a very similar power law relationship:

$$HWHM = 146(\omega^{-0.44}) \quad (30)$$

From the power law relationship, it appears that alignment may be a slightly stronger function of frequency than resulting shear rate, suggested by the larger exponent in Eq. (30).

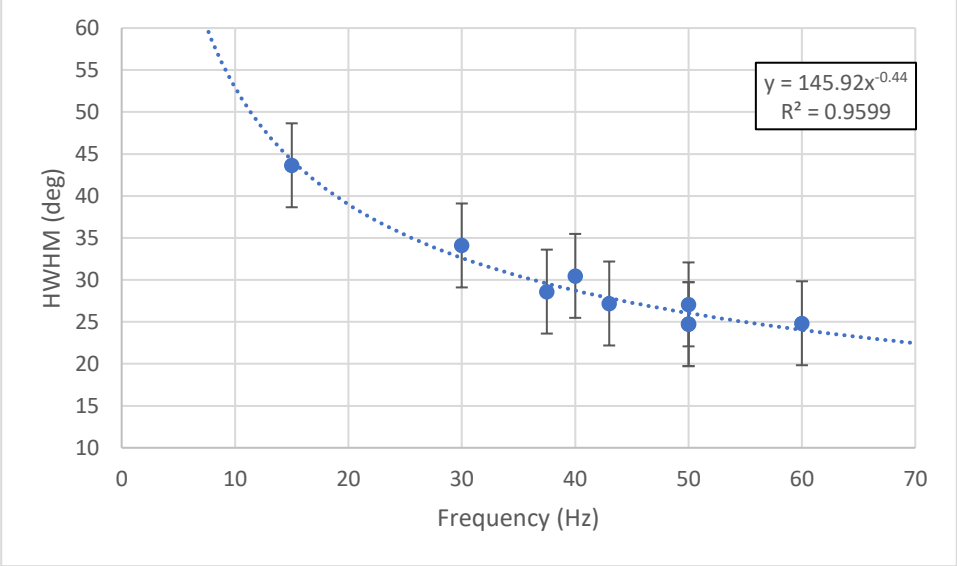

Figure 40: Half Width at Half Maximum as a function of Frequency for samples with a fixed amplitude of 1.5 mm and similar length distribution

For samples with a fixed frequency, the resulting shear rate can be varied by changing the amplitude. Figure 42 shows HWHM as a function of amplitude, or cam lift, for samples with a fixed frequency of 20 Hz.

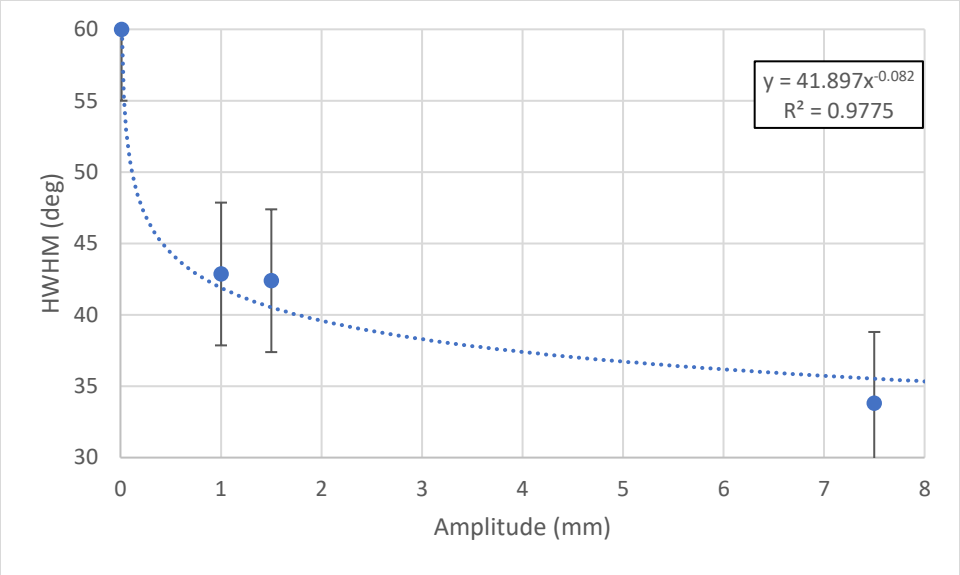

Figure 41: Half width at half maximum as a function of amplitude for samples with a fixed frequency of 20 Hz

From figure 42, it is evident that although alignment increases with amplitude, the relationship is much weaker than it is with frequency. A power law curve is fit to the data, given in Eq. (31):

$$HWHM = 41.9\ (A^{-0.08}) \tag{31}$$

From Eq. (31), it is clear that alignment is a weaker function of amplitude than it is of frequency, evidenced by the small exponent. However it is worth noting that less data is taken for this condition, and only one frequency was tested across multiple amplitudes. It is very possible that this relationship changes for higher frequencies / amplitudes.

3.1.1 Alignment – Length Relationship

Throughout data collection, depositions occurred over the course of several months, with many different batches of ink. These batches vary in many small ways such as the polymer CNT ratio, the total sonication time, the concentration, the *idle time*, and most importantly, the length

distribution. A consequence of these differences is that with enough data, the effect of different length distributions can be studied.

Fluid shear acts to align elongated particles by producing a shear force that acts on each particle to align its long axis with the flow direction. The force that induces this alignment is highly dependent on the shear rate and the rotational diffusion coefficient D_r of the particle [51]. The Péclet number is a dimensionless parameter that compares the magnitude of shear rate, γ, and the rotational diffusion coefficient:

$$Pe = \frac{\gamma}{D_r} \tag{32}$$

A Péclet number less than one implies that Brownian flocculation dominates, while a Péclet number greater than 1 implies the shear force is strong enough to influence the particle orientation [51]. The rotational diffusion coefficient is dependent on several factors such as temperature, particle size and aspect ratio, friction effects from the surrounding fluid, as well as the surrounding local concentration of particles. In the "free molecular regime", where the concentration of particles is assumed to be relatively small, and for nanoparticles with a high aspect ratio ($\beta > 100$), the rotational diffusion coefficient can be calculated approximately with:

$$D_r = \frac{k_b T\, K_n}{\pi \mu L_r^3 [\frac{1}{6} + f(\frac{\pi - 2}{48} + \frac{1}{8\beta})}} \tag{33}$$

Where k_b is the Boltzmann constant, K_n is the Knudeson number, T is the temperature, μ is the viscosity, L_r is the length of the nanoparticle, β is the aspect ratio, and f is the momentum accommodation [52]. From Eq. (33), it is clear that assuming a constant diameter, the rotational diffusion coefficient decreases with length of the rod raised to the third power, making it very sensitive to the length. This suggests that CNTs with a larger aspect ratio, or for a fixed diameter,

CNTs with a greater length, are more strongly affected by fluid shear and are more easily aligned in solution.

In order to quantify the effect of CNT length on alignment, the measured data is separated into bins with length ranges of 0.25 µm. For example, a bin labeled 5 µm contains all CNTs within 0.25 and 0.5 µm. For each group, the HWHM can be calculated, which allows the alignment to be plotted as a function of length. Figure 43 shows HWHM plotted as a function of nanotube length range for samples with amplitude of 1.5 mm and shear rate values of 3500, 6500, and 8600 s^{-1}. Also shown are the corresponding length distributions for each sample.

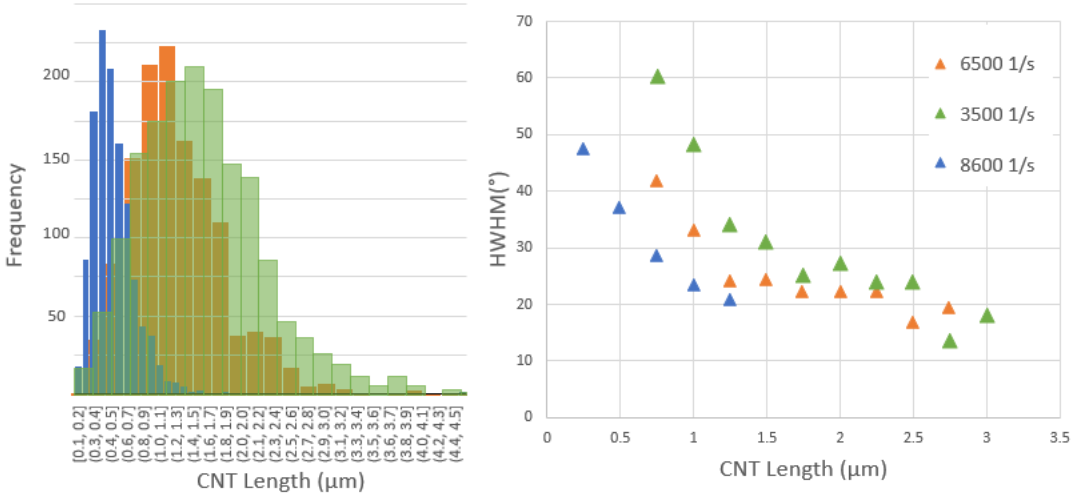

Figure 42: Half-width at half-maximum as a function of nanotube length (right) and the corresponding length distributions

From figure 43, several conclusions can be made. The first is that for all samples for CNTs below ~ 1.5 µm, alignment is a strong function of CNT length. All samples show approximately a 30° improvement in alignment with only ~1.25 µm increase in length from 0.25-1.5 µm. Beyond 1.5 µm, alignment continues to increase, but with diminishing returns. The second point that can be made is that despite the bulk measure of alignment for each sample

deviating from the trend that alignment increases with shear rate, for a given length range, greater shear rates correspond to better alignment. Between 0.75 and 1.5 µm, where all samples have a sufficient number of CNTs, the curves show a significant increase in alignment with shear rate. Clearly, the length of the CNTs in the ink is a major factor in the resulting alignment. Alignment appears best at lengths above 1.5 µm.

A further investigation is performed where two identical depositions are performed with separate CNT ink solutions with different length distributions. Both the length distribution and alignment distribution are displayed in figure 44. The shorter batch of CNTs is shown on the left in orange and the longer batch is shown on the right in blue.

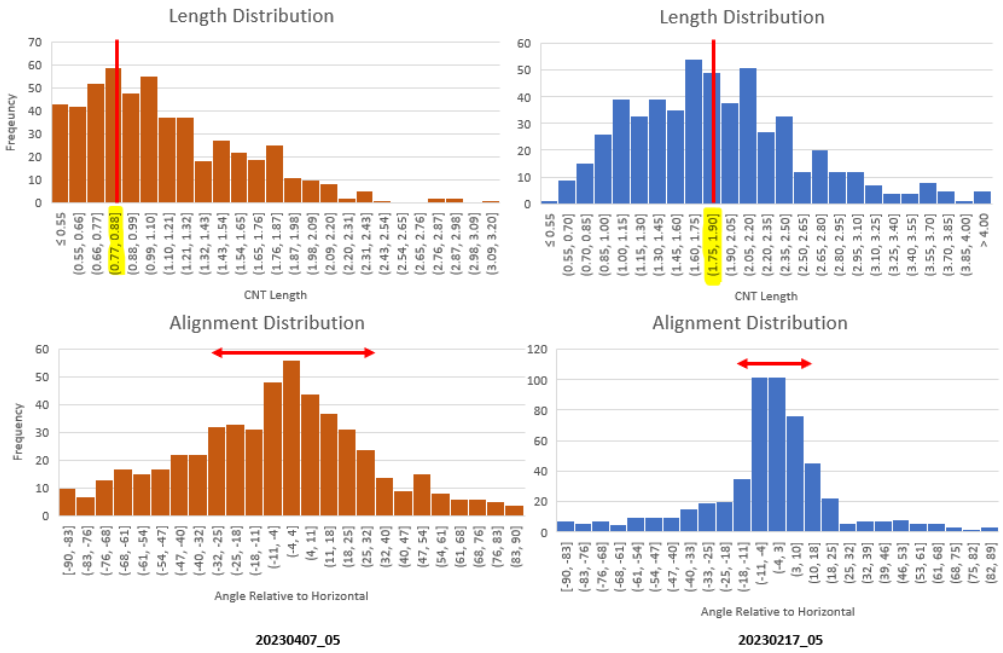

Figure 43: Length distribution and alignment distribution histograms for a sample with a low average CNT length (orange) and a longer average CNT length (blue)

The difference between the CNT length distributions can be clearly seen when comparing the top half of figure 44. The orange distribution has an average length near 0.8 µm and is

heavily right skewed. The blue distribution is also right-skewed, but to a much lesser extent, and has an average length of 1.8 µm. Also note the length of the tail in the blue distribution, and the presence of many CNTs > 3 µm in length, of which the orange batch has no CNTs over 3 µm. Focusing on the lower half of figure 44 shows a significant difference in the alignment distribution. The orange batch has a relatively flat curve which is slightly left-skewed but has long tails in either direction. This suggests a relatively normal distribution centered around 0°, with a gradually decreasing frequency of CNTs as the angle deviates from the horizontal. The blue batch has a much sharper peak centered around 0° (horizontal), and very small but long tails. This suggests a much greater fraction of CNTs clustered near 0° are aligned with the horizontal with fewer outliers point in random directions.

This analysis provides strong evidence that the shear force which acts to align elongated nanoparticles in solution more strongly affects those particles with a larger aspect ratio, or a greater length to diameter ratio. Future work may include a study in controlling CNT length to further improve alignment and to better understand the relationship between length and alignment.

4.5.2 Density

Another equally important characteristic of a CNT film is the packing density. High quality devices with good charge mobility require arrays with consistent pitch and an optimal packing density between 50-200 μm^{-1}[53,54]. Densities below this range often display low on-current and poor mobility [55], while densities too high can cause low on/off conductance modulation ratio [56,57].

Depending on the device application, various specific packing densities may be desired. Thus, control over packing density is a major benefit for any deposition method. Intuitively, the potential methods for controlling packing density in a method such as OSA would be varying the exposure time to CNT ink and the concentration of the ink. Here both methods are investigated to determine the effect of exposure time and concentration separately. Figure 45 shows the measured CNT linear packing density as a function of the cavity concentration.

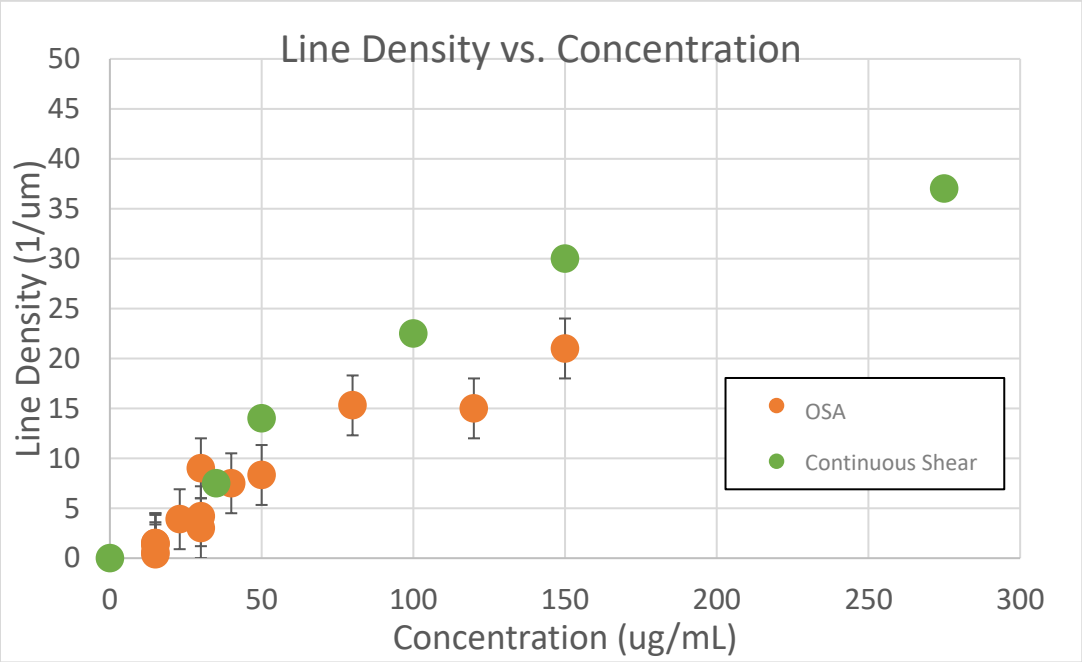

Figure 44: Linear packing density as a function of cavity concentration

It should be noted that the data presented here were collected with various oscillation frequencies and exposure times between 30 and 60 s, but a constant amplitude of 1.5 mm. A worst-case assumption for variation in the packing density is calculated and applied to all datapoints. Overlayed on figure 45 is the packing density data from continuous shear study for comparison [9]. Evidently the density appears to follow a similar power law relationship with

concentration, with large increases in packing densities occurring near lower concentrations, but diminishing returns as the concentration approaches 100-200 ug/mL. This is likely explained by the fact that as the surface becomes saturated with CNTs, it becomes more difficult for a new CNT to find an open spot to adhere to the substrate.

It is also interesting that the density achieved in OSA appears much lower than in the case of continuous shear. This could be a result of a depletion layer of decreased CNT concentration near a wall experiencing high oscillating shear rate. Similar depletion layers are observed in pressure-induced oscillatory flows when studying DNA particle concentration [42]. However, this is only conjecture and the true reason for this is unknown. Other possible reasons include differences in CNT ink preparation and surface preparation of the target substrate.

Intuitively, the density of deposited CNTs can be increased by increasing the cavity concentration, but CNT ink is expensive and time-consuming to manufacture, thus a solution which involves using less volume or lower concentrations of CNT are preferred. One way to achieve this is to increase the time a substrate is exposed to the CNT ink. However, repeated experiments show that beyond ~120 seconds of continuous exposure, the density begins to taper off. One way to circumvent this is to perform a deposition on a substrate, remove, clean, and bake it on a hot plate at 100°C for 10 minutes, then repeat the process. It is possible that long exposures to the CNT ink with chloroform solvent alters the surface chemistry of the substrate in a way that is unfavorable to CNT deposition. The cleaning and baking process may improve the surface to allow it to accept CNTs again, thus by performing multiple repeated depositions, it is possible to further increase the density of CNTs on the surface. Figure 46 shows a plot of areal density as a function of total exposure time for a single substrate with multiple repeated depositions.

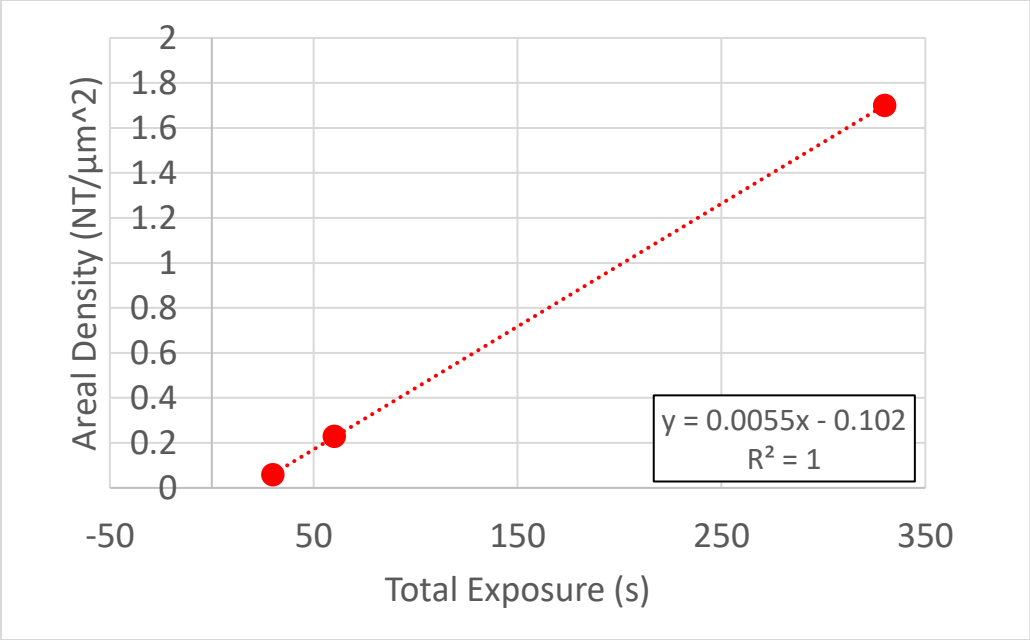

Figure 45: Areal density as a function of total exposure for repeated depositions

Figure 46 shows a strong linear relationship between the areal density deposited on the substrate and the total repeated exposure time in the range of exposures and density tested. It is expected that as higher areal densities are achieved, the slope of this line would decrease, and it would behave similarly to figure 45. It is also worth noting that these trials are performed with relatively low concentrations of ink (15 µg/mL), and thus yield low areal densities. Recall the desired packing density for most applications is 50-200 CNTs/µm. An approximate conversion from areal density to linear packing density by multiplying by the length of a single CNT implies that even at the highest areal density of 1.6 CNTs/µm^2, this corresponds to a line density of only 1.25 CNTs/µm. The important point here is that with repeated exposures, utilizing the cleaning and baking process described, multiple repeated depositions will increase CNT density on the substrate.

4.6 Conclusion

The experiments discussed here show that both alignment and packing density can be controlled with known parameters such as frequency, amplitude, CNT length, concentration, and exposure time, using the OSA method. Samples show achievable alignment of 25° HWHM and packing densities of 20 CNTs/μm. With improvements to the experimental setup, a better understanding of the deposition mechanics, and an understanding of the optimal solution space, OSA could likely be improved and scaled to yield samples with a high degree of alignment and moderate-high packing densities. The fast setup and deposition time, as well as the ability to reclaim and recover ink make OSA a promising potential method to produce wafer-scale alignment in the future.

5 Summary and Outlook

The work presented here explores several methods to produce aligned arrays of CNT films for use with carbon nanotube electronics. There is a specific focus on understanding the relationships that produce high quality films, such as with CNT length and alignment in OSA, as well as utilizing models to optimize and scale these methods, much like the tapered channel does for TaFISA. In addition, several image processing techniques are presented that have the potential to allow faster characterization of densely packed CNT films on a larger scale.

Some of the more noteworthy achievements are given below:

(1) A standard optical microscope fitted with a polarizer and analyzer can be used to create alignment maps of densely packed CNT films by rotating the sample and analyzing the resulting pixel intensities.

(2) Alignment degree and uniformity can be estimated using a single polarized optical microscopy image and analyzing the frequency and amplitude of the resulting intensity signal.

(3) With a modified apparatus, the TaFISA process can be applied to substrates to produce near full wafer coverage (~90%).

(4) Using a physics-based model of the TaFISA channel, the pooling behavior is simplified to a linear correlation for front distance which is a function of the pooling parameter (based on fluid properties), the gap width, and the friction factor.

(5) Alignment of CNTs and presumably other rod-like nanoparticles are highly influenced by length. Overall alignment can be improved significantly by producing CNT inks with lengths greater than 1.5 μm.

While these results are exciting, much more work can be done to expand upon the methods and modifications described here. Several topics where future work should be focused are:

(1) Gain a better understanding of the relationships between CNT film alignment degree and density to a resulting POM images intensity and color.
(2) Further investigate the optimal flow and lift rate conditions that produce high-quality, large-scale CNT films in the TaFISA process with a focus on repeatability.
(3) Utilize the OSA deposition method with CNT ink containing only long (> 1.5 μm) CNTs to achieve an even higher degree of global alignment.
(4) Perform experiments to test the time-dependent deposition rate of CNTs onto a substrate during the OSA deposition process, and how this can be improved to increase the resulting film density.

References

[1] Baughman, Ray H., Anvar A. Zakhidov, and Walt A. de Heer. “Carbon Nanotubes--the Route toward Applications.” *Science* 297, no. 5582 (2002): 787–92. https://doi.org/10.1126/science.1060928.

[2] Nurazzi, N. M., F. A. Sabaruddin, M. M. Harussani, S. H. Kamarudin, M. Rayung, M. R. Asyraf, H. A. Aisyah, et al. “Mechanical Performance and Applications of CNTS Reinforced Polymer Composites—a Review.” *Nanomaterials* 11, no. 9 (August 26, 2021): 2186. https://doi.org/10.3390/nano11092186.

[3] Ando, Tsuneya. “Electronic Properties of Carbon Nanotubes.” *Carbon Nanotubes*, October 21, 2009, 31–65. https://doi.org/10.1002/9783527618040.ch3.

[4] Yang, Feng, Meng Wang, Daqi Zhang, Juan Yang, Ming Zheng, and Yan Li. “Chirality Pure Carbon Nanotubes: Growth, Sorting, and Characterization.” *Chemical Reviews* 120, no. 5 (February 10, 2020): 2693–2758. https://doi.org/10.1021/acs.chemrev.9b00835.

[5] Tulevski, George S., Aaron D. Franklin, David Frank, Jose M. Lobez, Qing Cao, Hongsik Park, Ali Afzali, Shu-Jen Han, James B. Hannon, and Wilfried Haensch. “Toward High-Performance Digital Logic Technology with Carbon Nanotubes.” *ACS Nano* 8, no. 9 (2014): 8730–45. https://doi.org/10.1021/nn503627h.

[6] Franklin, Aaron D., Shu-Jen Han, George S. Tulevski, Mathieu Luisier, Chris M. Breslin, Lynne Gignac, Mark S. Lundstrom, and Wilfried Haensch. “Sub-10 Nm Carbon Nanotube Transistor.” *2011 International Electron Devices Meeting*, 2011. https://doi.org/10.1109/iedm.2011.6131600.

[7] Xu, Lin, Jie Yang, Chenguang Qiu, Shiqi Liu, Weijun Zhou, Qiuhui Li, Bowen Shi, et al. “Can Carbon Nanotube Transistors Be Scaled down to the Sub-5 Nm Gate Length?” *ACS Applied Materials & Interfaces* 13, no. 27 (2021): 31957–67. https://doi.org/10.1021/acsami.1c05229.

[8] Sinha, Sanjeet Kumar, and Saurabh Chaudhury. “Comparative Study of Leakage Power in CNTFET over MOSFET Device.” *Journal of Semiconductors* 35, no. 11 (2014): 114002. https://doi.org/10.1088/1674-4926/35/11/114002.

[9] Jinkins, Katherine R., Jason Chan, Robert M. Jacobberger, Arganthaël Berson, and Michael S. Arnold. “Substrate-wide Confined Shear Alignment of Carbon Nanotubes for Thin Film Transistors.” *Advanced Electronic Materials* 5, no. 2 (2018): 1800593. https://doi.org/10.1002/aelm.201800593.

[10] Jinkins, Katherine R., Jason Chan, Gerald J. Brady, Kjerstin K. Gronski, Padma Gopalan, Harold T. Evensen, Arganthaël Berson, and Michael S. Arnold. “Nanotube Alignment

Mechanism in Floating Evaporative Self-Assembly." *Langmuir* 33, no. 46 (2017): 13407–14. https://doi.org/10.1021/acs.langmuir.7b02827.

[11] Hedberg, James, Lifeng Dong, and Jun Jiao. "Air Flow Technique for Large Scale Dispersion and Alignment of Carbon Nanotubes on Various Substrates." *Applied Physics Letters* 86, no. 14 (2005). https://doi.org/10.1063/1.1897435.

[12] Lay, Marcus D., James P. Novak, and Eric S. Snow. "Simple Route to Large-Scale Ordered Arrays of Liquid-Deposited Carbon Nanotubes." *Nano Letters* 4, no. 4 (2004): 603–6. https://doi.org/10.1021/nl035233d.

[13] Zhao, Mengyu, Yahong Chen, Kexin Wang, Zhaoxuan Zhang, Jason K. Streit, Jeffrey A. Fagan, Jianshi Tang, et al. "DNA-Directed Nanofabrication of High-Performance Carbon Nanotube Field-Effect Transistors." *Science* 368, no. 6493 (2020): 878–81. https://doi.org/10.1126/science.aaz7435.

[14] Liu, Lijun, Jie Han, Lin Xu, Jianshuo Zhou, Chenyi Zhao, Sujuan Ding, Huiwen Shi, et al. "Aligned, High-Density Semiconducting Carbon Nanotube Arrays for High-Performance Electronics." *Science* 368, no. 6493 (2020): 850–56. https://doi.org/10.1126/science.aba5980.

[15] Cao, Qing, Shu-jen Han, George S. Tulevski, Yu Zhu, Darsen D. Lu, and Wilfried Haensch. "Arrays of Single-Walled Carbon Nanotubes with Full Surface Coverage for High-Performance Electronics." *Nature Nanotechnology* 8, no. 3 (2013): 180–86. https://doi.org/10.1038/nnano.2012.257.

[16] Jinkins, Katherine R., Sean M. Foradori, Vivek Saraswat, Robert M. Jacobberger, Jonathan H. Dwyer, Padma Gopalan, Arganthaël Berson, and Michael S. Arnold. "Aligned 2d Carbon Nanotube Liquid Crystals for Wafer-Scale Electronics." *Science Advances* 7, no. 37 (2021). https://doi.org/10.1126/sciadv.abh0640.

[17] Vig, John R. *UV/ozone cleaning of surfaces*, January 1, 1992. https://doi.org/10.21236/ada169024.

[18] Kalisky, Beena, Eric M. Spanton, Hilary Noad, John R. Kirtley, Katja C. Nowack, Christopher Bell, Hiroki K. Sato, et al. "Locally Enhanced Conductivity Due to the Tetragonal Domain Structure in LAALO3/SRTIO3 Heterointerfaces." *Nature Materials* 12, no. 12 (September 8, 2013): 1091–95. https://doi.org/10.1038/nmat3753.

[19] DeCamp, Stephen J., Gabriel S. Redner, Aparna Baskaran, Michael F. Hagan, and Zvonimir Dogic. "Orientational Order of Motile Defects in Active Nematics." *Nature Materials* 14, no. 11 (November 17, 2015): 1110–15. https://doi.org/10.1038/nmat4387.

[20] Wilde, H. D. “Two Forms of a Constant Water–Level Device.” *Industrial & Engineering Chemistry* 16, no. 9 (September 1924): 904–904. https://doi.org/10.1021/ie50177a010.

[21] Edomwonyi-Otu, Lawrence C., and Panagiota Angeli. “Pressure Drop and Holdup Predictions in Horizontal Oil–Water Flows for Curved and Wavy Interfaces.” *Chemical Engineering Research and Design* 93 (2015): 55–65. https://doi.org/10.1016/j.cherd.2014.06.009.

[22] Keulegan, G.H. “Laminar Flow at the Interface of Two Liquids.” *Journal of Research of the National Bureau of Standards* 32, no. 6 (1944): 303. https://doi.org/10.6028/jres.032.016.

[23] Burton, J. C., F. M. Huisman, P. Alison, D. Rogerson, and P. Taborek. “Experimental and Numerical Investigation of the Equilibrium Geometry of Liquid Lenses.” *Langmuir* 26, no. 19 (2010): 15316–24. https://doi.org/10.1021/la102268n.

[24] Pujado, P.R, and L.E Scriven. “Sessile Lenticular Configurations: Translationally and Rotationally Symmetric Lenses.” *Journal of Colloid and Interface Science* 40, no. 1 (1972): 82–98. https://doi.org/10.1016/0021-9797(72)90175-0.

[25] Phan, Chi M. “Stability of a Floating Water Droplet on an Oil Surface.” *Langmuir* 30, no. 3 (2014): 768–73. https://doi.org/10.1021/la403830k.

[26] Vella, Dominic, Duck-Gyu Lee, and Ho-Young Kim. “The Load Supported by Small Floating Objects.” *Langmuir* 22, no. 14 (2006): 5979–81. https://doi.org/10.1021/la060606m.

[27] Tavana, Hossein, Guocheng Yang, Christopher M. Yip, Dietmar Appelhans, Stefan Zschoche, Karina Grundke, Michael L. Hair, and A. Wilhelm Neumann. “Stick−slip of the Three-Phase Line in Measurements of Dynamic Contact Angles.” *Langmuir* 22, no. 2 (2005): 628–36. https://doi.org/10.1021/la051715o.

[28] Hager, Willi H. “Wilfrid Noel Bond and the Bond Number.” *Journal of Hydraulic Research* 50, no. 1 (2012): 3–9. https://doi.org/10.1080/00221686.2011.649839.

[29] Padding, Johan T., Niels G. Deen, E.A.J.F. (Frank) Peters, and J.A.M. (Hans) Kuipers. “Euler–Lagrange Modeling of the Hydrodynamics of Dense Multiphase Flows.” *Mesoscale Modeling in Chemical Engineering Part I*, 2015, 137–91. https://doi.org/10.1016/bs.ache.2015.10.005.

[30] Rapp, Bastian E. “Chapter 21 - Capillarity.” Essay. In *Microfluidics: Modelling, Mechanics and Mathematics*, 445–51. Elsevier, 2017.

[31] Xiang, Hong Wei. “Chapter 8 - Surface Tension.” Essay. In *The Corresponding-States Principle and Its Practice: Thermodynamics, Transport and Surface Properties of Fluids*, 215–28. Amsterdam: Elsevier, 2005.

[32] White, Frank M., and Henry Xue. “Chapter 6 - Viscous Flow in Ducts .” Essay. In *Fluid Mechanics*, 347–84. New York, NY: McGraw-Hill, 2021.

[33] Traciak, Julian, and Gaweł Żyła. “Effect of Nanoparticles Saturation on the Surface Tension of Nanofluids.” *Journal of Molecular Liquids* 363 (2022): 119937. https://doi.org/10.1016/j.molliq.2022.119937.

[34] Li, Xiaoke, Wenjing Chen, and Changjun Zou. “The Stability, Viscosity and Thermal Conductivity of Carbon Nanotubes Nanofluids with High Particle Concentration: A Surface Modification Approach.” *Powder Technology* 361 (2020): 957–67. https://doi.org/10.1016/j.powtec.2019.10.106.

[35] Nellis, Gregory, and Sanford Klein. “Internal Forced Convection.” Essay. In *Heat Transfer*, 638. Cambridge: Cambridge University Press, 2012.

[36] Bullard, Jeffrey W., and Edward J. Garboczi. “Capillary Rise between Planar Surfaces.” *Physical Review E* 79, no. 1 (2009). https://doi.org/10.1103/physreve.79.011604.

[37] Ratnesh, R.K., A. Goel, G. Kaushik, H. Garg, Chandan, M. Singh, and B. Prasad. “Advancement and Challenges in MOSFET Scaling.” *Materials Science in Semiconductor Processing* 134 (November 2021): 106002. https://doi.org/10.1016/j.mssp.2021.106002.

[38] Daneshvar, Farhad, Hengxi Chen, Kwanghae Noh, and Hung-Jue Sue. “Critical Challenges and Advances in the Carbon Nanotube–Metal Interface for next-Generation Electronics.” *Nanoscale Advances* 3, no. 4 (January 2021): 942–62. https://doi.org/10.1039/d0na00822b.

[39] Kanoun, Olfa, Christian Müller, Abderahmane Benchirouf, Abdulkadir Sanli, Trong Dinh, Ammar Al-Hamry, Lei Bu, Carina Gerlach, and Ayda Bouhamed. “Flexible Carbon Nanotube Films for High Performance Strain Sensors.” *Sensors* 14, no. 6 (June 6, 2014): 10042–71. https://doi.org/10.3390/s140610042.

[40] Kunaraj, Arulampalam, P. Chelvanathan, Ahmad Ashrif A Bakar, and Iskandar Yahya. “Single-Walled Carbon Nanotube (SWCNT) Thin Films via Automatic Spray Coating and Nitric Acid Vapor Treatment.” *Journal of Engineering Research*, July 2023. https://doi.org/10.1016/j.jer.2023.07.002.

[41] Saotome, Tsuyoshi, Hansang Kim, Zhe Wang, David Lashmore, and H. Thomas Hahn. “Transparent Conducting Film: Effect of Vacuum Filtration of Carbon Nanotube Suspended in Oleum.” *Bulletin of Materials Science* 34, no. 4 (July 2011): 623–28. https://doi.org/10.1007/s12034-011-0172-7.

[42] Jo, Kyubong, Yeng-Long Chen, Juan J. de Pablo, and David C. Schwartz. “Elongation and Migration of Single DNA Molecules in Microchannels Using Oscillatory Shear Flows.” *National Library of Medicine* 9, no. 16 (June 10, 2009): 2348. https://doi.org/10.1039/b902292a.

[43] Elder, Brian, Rajan Neupane, Eric Tokita, Udayan Ghosh, Samuel Hales, and Yong Lin Kong. “Nanomaterial Patterning in 3D Printing.” *Advanced Materials* 32, no. 17 (March 4, 2020): 1907142. https://doi.org/10.1002/adma.201907142.

[44] Zhao, Chuangqi, Pengchao Zhang, Jiajia Zhou, Shuanhu Qi, Yoshihiro Yamauchi, Ruirui Shi, Ruochen Fang, et al. “Layered Nanocomposites by Shear-Flow-Induced Alignment of Nanosheets.” *Nature* 580, no. 7802 (May 8, 2020): 210–15. https://doi.org/10.1038/s41586-020-2161-8.

[45] Alizadehgiashi, Moien, Amir Khabibullin, Yunfeng Li, Elisabeth Prince, Milad Abolhasani, and Eugenia Kumacheva. “Shear-Induced Alignment of Anisotropic Nanoparticles in a Single-Droplet Oscillatory Microfluidic Platform.” *Langmuir* 34, no. 1 (December 18, 2017): 322–30. https://doi.org/10.1021/acs.langmuir.7b03648.

[46] “Design of Cam Profile in Matlab.” Xdynemo, May 31, 2021. https://xdynemo.wordpress.com/design-of-cam-profile-in-matlab/.

[47] Khaled, A.-R.A., and K. Vafai. “The Effect of the Slip Condition on Stokes and Couette Flows Due to an Oscillating Wall: Exact Solutions.” *International Journal of Non-Linear Mechanics* 39, no. 5 (July 2004): 795–809. https://doi.org/10.1016/s0020-7462(03)00043-x.

[48] Gersten, K. “Unsteady Plane Flows - Flow at an Oscillating Wall (Stokes Second Problem).” Essay. In *Boundary Layer Theory*, 129–39. New York, Springer-Verlag, 2003.

[49] Dwyer, Jonathan H., Anjali Suresh, Katherine R. Jinkins, Xiaoqi Zheng, Michael S. Arnold, Arganthaël Berson, and Padma Gopalan. “Chemical and Topographical Patterns Combined with Solution Shear for Selective-Area Deposition of Highly-Aligned Semiconducting Carbon Nanotubes.” *Nanoscale Advances* 3, no. 6 (February 17, 2021): 1767–75. https://doi.org/10.1039/d1na00033k.

[50] Miller, Chester. “Predicting Non-Newtonian Flow Behavior in Ducts of Unusual Cross Section.” *Industrial & Engineering Chemistry Fundamentals* 11, no. 4 (November 1, 1972): 524–28. https://doi.org/10.1021/i160044a015.

[51] Calabrese, Vincenzo, Stylianos Varchanis, Simon J. Haward, and Amy Q. Shen. “Alignment of Colloidal Rods in Crowded Environments.” *Macromolecules* 55, no. 13 (June 29, 2022): 5610–20. https://doi.org/10.1021/acs.macromol.2c00769.

[52] Li, Mingdong, George W. Mulholland, and Michael R. Zachariah. “Rotational Diffusion Coefficient (or Rotational Mobility) of a Nanorod in the Free-Molecular Regime.” *Aerosol Science and Technology* 48, no. 2 (December 13, 2013): 139–41. https://doi.org/10.1080/02786826.2013.864752.

[53] 6G. S. Tulevski, A. D. Franklin, D. Frank, J. M. Lobez, Q. Cao, H. Park, A. Afzali, S.-J. Han, J. B. Hannon, W. Haensch, *ACS Nano* 2014, 8, 8730.

[54] C. Rutherglen, D. Jain, P. Burke, *Nat. Nanotechnol.* 2009, 4, 811.

[55] 13I. V. Zaporotskova, N. P. Boroznina, Y. N. Parkhomenko, L. V. Kozhitov, *Mod. Electron. Mater.* 2016, 2, 95.

[56] 10G. J. Brady, K. R. Jinkins, M. S. Arnold, *J. Appl. Phys.* 2017, 122, 124506.

[57] 12V. Perebeinos, J. Tersoff, *Phys. Rev. Lett.* 2015, 114, 085501.